# A Streamlined Test-Oriented Lifetime Assessment Framework for Automotive Power Electronics Converters

Sachin Kumar Bhoi, *Member, IEEE*, Sajib Chakraborty, *Member, IEEE*, Alireza Aghdaei, *Graduate Student Member, IEEE*, Anu Mathew, Tobias Daniel Horn, Sebastian Liebig, Jan Albrecht, Christoph Abart, Rik W. De Doncker, *Fellow, IEEE*, and Omar Hegazy, *Senior Member, IEEE*

***Abstract*—Automotive power electronics are critical components in electric vehicles (EVs), forming the backbone of the powertrain, where their performance and durability directly impact overall vehicle reliability. Current state-of-the-art lifetime testing and modeling methods for power electronics converters (PECs) rely on extensive experimental testing and/or high-fidelity physics-based models to assess degradation over the vehicle's lifetime, which is both resource-intensive and time-consuming. Consequently, there is increasing demand from automotive original equipment manufacturers (OEMs) to incorporate reliability and lifetime evaluation in the early design phases of PECs, such as dc–dc converters and power inverters, prior to entering series production. To address this challenge, this article proposes a streamlined methodology for testing, modeling, and lifetime assessment of a 150 kW silicon carbide-based traction inverter. The inverter is tested on an industry-grade automotive test bench across multiple driving profiles. Accurate multiphysics modeling is performed using the test data, focusing on electrothermal models for bond-wire degradation and thermomechanical models for die-attach degradation. A reliability assessment model integrates these multiphysics modeling results with statistical lifetime estimation. Lifetime assessments across various driving profiles reveal the influence of profile characteristics on reliability, highlighting that bond-wire degradation accounts for 91% of total lifetime degradation, while die-attach failure contributes only 9%. This work demonstrates that a systematic, test-driven methodology, combined with a collaborative lifetime assessment framework, significantly enhances confidence in the design of automotive power electronics. The proposed framework can be seamlessly integrated into the early design phase to optimize design outcomes and accelerate the design-to-market process. Compared to a conventional high-fidelity model-based approach, the proposed framework reduces mission-profile-based lifetime assessment effort by approximately 90%.***

***Index Terms*—Lifetime testing, mission profile, multiphysical model, power electronics, reliability.**

## I. Introduction

THE shift to electrified mobility has positioned power electronics converters (PECs) as a critical component. Electric vehicles (EVs) rely heavily on PECs, including inverters, onboard chargers (OBCs), and direct current (dc)–dc converters, to support complex, power-dense architectures. The automotive power electronics market (excluding battery cells) is projected to grow at a 15% compound annual growth rate (CARG) from 2020 to 2030, reaching approximately a market size of $85 billion [1].

The main engineering challenge is to achieve high reliability and efficiency at minimal cost, particularly in safety-critical PEC, such as an automotive inverter. Automotive OEMs demand near-zero defect rates, continuous operation over 10+ years or 300 000 miles (approx. 480 000 km), and reliable performance in a wide ambient temperature range from –40 °C to +150 °C [2]. As a result, PECs are subjected to elevated thermal, electrical, and mechanical stresses throughout their operating lifetime [3]. Various recent automotive industry recalls highlight PECs reliability issues: Toyota recalled Prius models in 2014 for overheating intelligent power modules (IPMs) in inverters [4], Chrysler recalled 2017 pacifica plug-in hybrid EVs for IPM diode failures [5], Tesla recalled over 2000 Cybertrucks in 2024 for inverter semiconductor defects [6], and Hyundai recalled over 145 000 EVs for integrated charging control unit failures [7]. Besides, a report by consumer reports in 2023 reveals that EVs are, on average, less reliable than their internal combustion engine counterparts [8].

Real-world failures and the growing complexity of EVs architectures underscore the urgent need for reliability and lifetime

Received 17 June 2025; revised 14 August 2025 and 7 October 2025; accepted 2 November 2025. Date of publication 10 November 2025; date of current version 19 January 2026. This work was supported in part by the HiPower5.0 project, which is supported in part by the Chips Joint Undertaking and its members, including the top-up funding by Austria, Belgium, the Czech Republic, Denmark, France, Germany, Italy, The Netherlands, Slovakia, and Slovenia. The HiPower 5.0 Project under Grant 101194250 and co funded by the European Union, and in part by the HiEFFICIENT project under Grant 101007281. Recommended for publication by Associate Editor D. Peftitsis. *(Corresponding author: Sajib Chakraborty.)*

Sachin Kumar Bhoi, Sajib Chakraborty, and Omar Hegazy are with MOBI-EPOWERS Research Group, ETEC Department, Vrije Universiteit Brussel (VUB), 1050 Brussel, Belgium, and also with Flanders Make, 3001 Heverlee, Belgium (e-mail: sajib.chakraborty@vub.be).

Alireza Aghdaei and Rik W. De Doncker are with the Institute for Power Electronics, Electrical Drives, RWTH Aachen University, 52062 Aachen, Germany.

Anu Mathew, Tobias Daniel Horn, and Jan Albrecht are with the Fraunhofer Institute for Electronic Nanosystems (ENAS), 09126 Chemnitz, Germany.

Sebastian Liebig is with AVL-SET GmbH, 88239 Wangen, Germany.

Christoph Abart is with AVL List GmbH, 8020 Graz, Austria.

Color versions of one or more figures in this article are available at https://doi.org/10.1109/TPEL.2025.3630790.

Digital Object Identifier 10.1109/TPEL.2025.3630790

© 2025 The Authors. This work is licensed under a Creative Commons Attribution 4.0 License. For more information, see https://creativecommons.org/licenses/by/4.0/

TABLE I
COMPARATIVE OVERVIEW OF LITERATURE ON THE RELIABILITY ASSESSMENT OF PECs

| Ref. | Components | System | Reliability Assessment | | | | | | |
|---|---|---|---|---|---|---|---|---|---|
| | | | Lifetime Model Assessment | | | | Failure Precursor Data | | |
| | | | Failure Precursor Data | Simulation Model | | Lifetime Model | Mission Profile | | Data Sampling Rate |
| | | | | Electro-Thermal | Thermo-Mechanical | | Type | Duration | |
| [10] | SiC MOSFET | Interleaved dc–dc converter | Rds On | NA | NA | Markov Chain Analysis | No mission profile base analysis. Lifetime extension based on experimental setup | | |
| [11] | | | $T_j$ | ✓ | × | Scheuermann | Driving Cycles | 6500s | 100Hz |
| [12] | | | $T_j$ | ✓ | × | | | 6800s | 10Hz |
| [13] | IGBT, Diode, Capacitor, Battery | Hybrid EV Drive | $T_j$ | ✓ | × | RDF 200 | | 1965s | NA |
| [14] | MOSFET | Automotive Traction Inverter | $T_j$ | ✓ | × | LESIT | | NA | 1Hz |
| [15] | SiC MOSFET | Rectifier | $T_j$,I-phase | ✓ | ✓ | Plastic Strain Model | | 1800s | NA |
| [16] | IGBT | Three Level PV Inverter | $T_j$ | ✓ | × | Bayerer (CIPS 2008) | Solar Profile | 1 year | 1 min |
| [17] | IGBT | PV Inverter | $T_j$ | ✓ | × | Bayerer (CIPS 2008) | | 12hr | NA |
| [18] | IGBT | PV Inverter | $T_j$ | ✓ | × | Bayerer (CIPS 2008) | | 1 year | 1Hz |
| [19] | IGBT | PV Power Converter | $T_j$ | ✓ | × | Scheuermann | | 1 year | 5 min |
| [20] | IGBT | Wind Power Converter | $T_j$ | ✓ | × | Semikron IGBT Model | Wind Profile | 1 year | 3h, 1s, 0.5ms |
| [21] | IGBT | Traction Inverter | $T_j$ | ✓ | × | LESIT | Speed Profile | 100s | NA |
| [22] | IGBT | Electric Drive Inverter | $T_j$ | ✓ | × | Scheuermann | | 1000s | 0.1Hz |
| [23] | MOSFET | eBike Inverter | $T_j$ | NA | NA | Machine Learning | Field Data | 110 min | 10Hz |
| [24] | IPOSIM (Infineon) Tool | | $T_j$ | ✓ | × | NA | Selectable | | |
| [26] | IGBT, Capacitor | dc–dc Charger | $T_j$ | ✓ | × | Bayerer (CIPS 2008) | Charging load profile | 60 min | NA |
| [25] | IGBT, Capacitor | Fast charging station | $T_j$ | ✓ | × | Scheurmann | Charging profile | 1200s | NA |
| [27] | SiC MOSFET | Inverter | $T_j$, I-phase | ✓ | ✓ | Plastic Strain Model | Driving Cycles | 1800s | NA |
| This article | SiC MOSFET | Automotive Traction Inverter | $T_j$, I-phase | ✓ | ✓ | Scheuermann , Plastic Strain Model | Driving Cycles | 4148s | 1kHz |

∗ Summary of various lifetime model mentioned in the table, along with their mathematical equation, can be found in [29].

assessment during the early design phase of automotive PECs. Power semiconductor switches—the most failure-prone components within PECs—account for nearly 31% of failures [9]. The increasing use of wide bandgap (WBG) materials, such as silicon carbide (SiC) and gallium nitride (GaN), further contributes to PEC unreliability. Previous lifetime assessment studies follow a consistent approach, as summarized in Table I, which also compares them with the approach adopted in this work. Most studies employ high-fidelity PEC switching transient models in combination with power switch models to evaluate power losses, followed by electrothermal models to estimate Junction temperature ($T_j$)-a key failure precursor. This precursor, combined with standard lifetime models, estimate PEC useful life [10], [11], [12], [13], [14], [15], [16], [17], [18], [19], [20], [21], [22], [23], [24], [25], [26], [27]. While effective for predesign analysis, this approach relies heavily on manufacturer-provided switch models, is computationally intensive due to submicrosecond simulation timesteps [28], and overlooks heatsink design, cooling systems, and prototype testing feedback during PEC design. Without incorporating prototype testing data, the assessment is limited to predesign, hindering continuous optimization for design-for-reliability (DfR).

Targeted component-level reliability testing provides insight into degradation mechanisms under defined thermal and electrical stress. Hosseinabadi et al. [29] outlined major failure mechanisms of power semiconductor devices at both chip and package levels. A recent investigation of discrete Insulated-gate bipolar transistor (IGBT) switches under power cycling with

low temperature swings and varying on-times revealed that the number of cycles to failure increases as on-time decreases, using a 5% increase in forward voltage as the failure criterion, with wire bond lift-off and heel crack identified as the dominant failure modes. Component-level reliability testing follows established qualification standards, such as JEDEC JESD47, IEC 60068, and MIL-HDBK-217F, with automotive-specific standards, such as AEC-Q100 (integrated circuits), AEC-Q101 (discrete semiconductors), AEC-Q200 (passive components), AEC-Q104 (multichip modules), and AQG 324 (power semiconductor modules) tailored for the harsh conditions of traction applications [29]. Despite these standards, lifetime testing for automotive PEC heavily depends on prototype vehicles and hardware-in-the-loop test benches that simulate end-of-life behavior through accelerated mileage. These approaches are resource-intensive, demanding extensive infrastructure and multiple hardware iterations. Consequently, there is growing demand for shorter testing cycles, ideally 2 to 3 months, to validate series production components like inverters, OBCs, and dc–dc converters under realistic mission conditions. While aerospace industries use highly accelerated life testing (HALT) and highly accelerated stress screening, their cost-proprietary nature limits their use in automotive settings [30].

Current automotive testing setups, such as passive loads, back-to-back converter configurations, and e-motor emulators, are constrained by streamlined workflows, limited data exchange between physical and virtual environments (e.g., simulations), and high operational costs. This reveals a clear gap in seamlessly integrating lifetime testing data into downstream simulation, modeling, and lifetime assessment.

To address the above-mentioned limitations of current PEC testing and lifetime modeling, this article proposes a test-oriented lifetime assessment framework for automotive PECs that introduces a digital infrastructure for reliable, cost-efficient reliability evaluation. This new paradigm integrates automated test execution on a test bench, accurately emulating e-motor dynamics at PEC terminals, with seamless data exchange for multiphysics cosimulation and a statistical lifetime assessment model. By bridging experimental test data with model-based assessment, it standardizes lifetime testing methodology. This framework embeds into the design and prototyping phases, enabling DfR before PEC series production. This work also makes several contributions to lifetime assessment for power electronics semiconductor devices in PECs, in the proposed framework, as outlined in the following.

1) The majority of studies outlined in Table I rely on $T_j$ as the primary indicator for bond-wire degradation in power semiconductors [10], [11], [12], [13], [14], [15], [16], [17], [18], [19], [20], [21], [22], [23], [24], [25], [26], [27]. However, a recent power cycling experiment conducted by one of the authors revealed two key failure mechanisms: bond-wire lift, occurring at the package level, and die attach failure, occurring at the chip level [31]. To address both, the proposed lifetime assessment framework integrates an electrothermal model to estimate $T_j$ for bond-wire degradation analysis and an electro-thermomechanical model to compute inelastic strain at the die attach solder joint for failure analysis. These multidomain failure mechanisms are combined within the framework using separate lifetime models for each damage type. This approach, which merges multiple failure mechanisms and precursors, represents a novel contribution to the automotive PEC reliability assessment.
2) High-fidelity PEC switching transient model simulations require timesteps as low as tens of nanoseconds to capture switching behavior and calculate power losses. A study for EV shows that it takes 15 minutes of time in an Intel i7 processor for full vehicle-level simulation of 1 ms at a timestep of 1 $\mu$s [28]. These computational demands limit the utilization of mission profile simulations in the automotive sector. This article addresses this by deriving a loss model from test data, using established physical equations and curve fitting for device-level nonlinearities. The test data directly informs electrothermal and electro-thermomechanical models, eliminating the need for a high-fidelity full inverter simulation model. Computationally intensive models are simplified using surrogate modeling with functional mock-up unit (FMU) for integration into the proposed framework. The methodology seamlessly combines prototype test data, modeling, and degradation precursor derivation for PEC reliability assessment. After initial modeling, the process need not be repeated for DfR, as the modeling and lifetime assessment tool directly uses test data to provide feedback to hardware designers on reliability analysis outcomes. Thus, demonstration of the advantages of the streamlined workflow with regard to a reduction in development and assessment efforts, and provides the ability for earlier DfR validation (when there is still significant design freedom).
3) Third, a compact lifetime assessment model development is shown, which conducts statistical reliability analysis at both component and system levels, providing the probability of failure for the automotive PEC relative to driving distance. Notably, the model incorporates bond wire degradation and die attach failure degradation of the SiC MOSFET. Lifetime evaluation is performed using three standard driving profiles: worldwide harmonized light vehicle test procedure (WLTP), new european driving cycle (NEDC), and JC08. The influence of the driving profile is distinctly evident in the lifetime assessment outcomes.

The rest of this article is organized as follows. Section II introduces the proposed concept, while Section III details the automotive lifetime testbench, which employs industry-standard testing across various standard driving cycles for the unit under test (UUT). Section IV elaborates on the development of electrothermal and electro-thermomechanical simulation models to estimate failure precursors. Section V provides a step-by-step explanation of the combined lifetime assessment model developed for lifetime estimation. Section VI presents the results from the compact lifetime assessment model, including a comparison of lifetime estimations of various mission profile data obtained from the test bench. Finally, Section VII concludes this article.

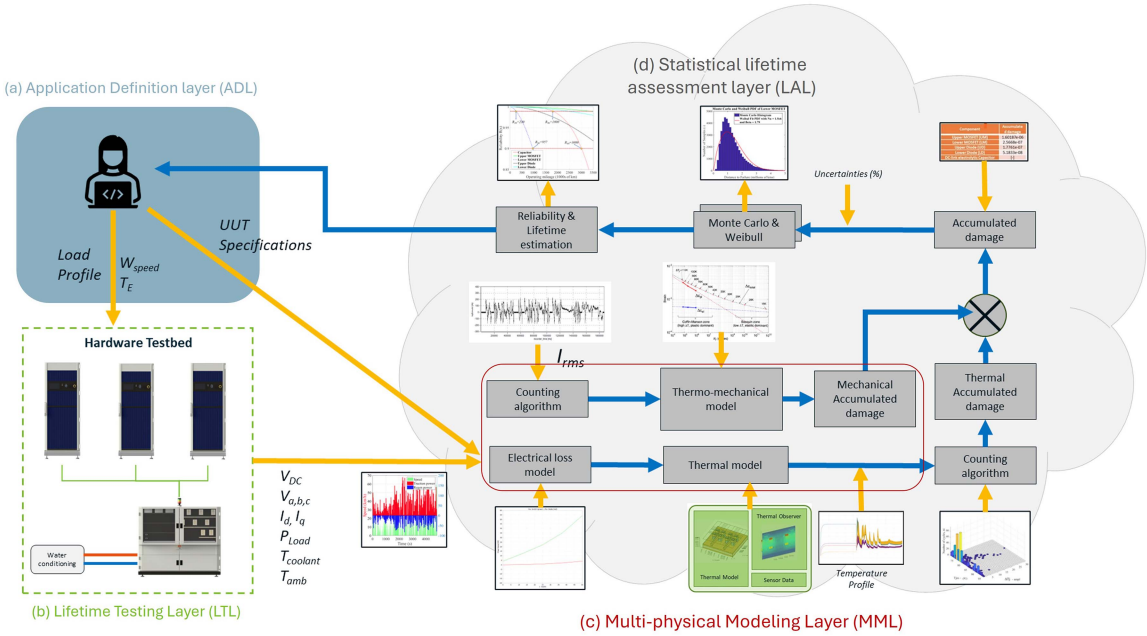


Fig. 1. The Test-oriented lifetime assessment approach for automotive PECs comprises four semantic layers. a) Application Definition Layer (ADL). (b) Lifetime Testing Layer (LTL). (c) Multiphysical Modelling Layer (MML). (d) Statistical Lifetime Assessment Layer (LAL).

## II. Proposed Concept

In the following section, the main approach and methodology for the proposed framework are outlined step-by-step. The overall method is categorized into the following four distinct layers:

1) application definition layer (ADL);
2) lifetime testing layer (LTL);
3) multiphysical modeling layer (MML); and
4) statistical lifetime assessment layer (LAL).

The ADL Fig. 1(a) serves as the core software layer in the proposed framework, managing the testing, multiphysics modeling, and lifetime assessment tool, semantically to ensure interoperability. The three primary functions of the ADL are: determining the testing methodology; delineating the UUT, including the system requirements and operational conditions within the EV; and selecting mission profiles and automated vehicle-level simulation for load profile extraction for the UUT testing. Furthermore, the ADL facilitates an interface for data storage, automated test execution, and seamless data exchange with the MML and LAL.

In the ADL, the testing approach is rigorously selected in accordance with established standards and procedures applicable at both the component and system levels, with particular emphasis on IEEE Standard 1332-2012 [32]. This standardization ensures methodological consistency and aligns the testing framework with industry best practices, enhancing the credibility and acceptance of the testing outcomes. Typically, automotive OEMs and Tier-1 suppliers rely on two primary testing approaches: white box testing and black box testing. These approaches provide different levels of system insight and data accessibility, influencing the selection of testing strategies and model integration within the ADL framework.

1) *White box testing:* This approach provides comprehensive knowledge of system details, including topology, power switch specifications, dc-link characteristics, sensor configurations, geometries, and on module level electrical, thermal, and mechanical characteristics of material and semiconductor devices. The UUT remains accessible, enabling data to be recorded at different sampling rates according to model requirements. With such detailed information, the entire system can be accurately modeled, facilitating the development of reliable testing methodologies [33].
2) *Black box testing:* In this approach, only basic information and global signals, such as input/output voltage, current and power levels remain available, with no insights into the internal electronic components and no physical access to the UUT [34]. Due to this lack of system-level details, achieving sufficient accuracy in testing methodologies and having sufficient data for models presents a significant challenge.

Therefore, to have an appropriate and acceptable lifetime test methodology for automotive PEC, in this article, a white box testing approach has been chosen. Moreover, the target is to set up an appropriate test framework with a white box system first, to be able to validate the designed approach, and second, to transform the methodology toward the black box application and validate it.

After selecting the testing approach, the UUT is identified. In this study, the drive inverter is chosen as the UUT, as it is a mandatory PEC in every EV and a critical element of the powertrain. The drive inverter functions as an intelligent control unit, converting dc of the battery into rotating multiphase alternating current (ac), thereby enabling precise torque control of the electric motor (e-motor).

TABLE II
KEY PARAMETERS OF THE CONSIDERED MISSION PROFILE FOR LIFETIME TESTING OF THE UUT

| Speed Profile | Characteristics |
|---|---|
| WLTP | Cycle length = 23.27 km, Duration = 30 min, Max Speed = 131.3 km/h, Average Speed = 46.5 km/h, Start/Stop = Frequent |
| NEDC | Cycle length = 11.03 km, Duration = 19.6 min, Max Speed = 120 km/h, Average Speed = 33.6 km/h, Start/Stop = Moderate |
| Japanese JC08 Cycle (JC08) | Cycle length = 8.17 km, Duration = 20 min, Max Speed = 81.6 km/h, Average Speed = 24.4 km/h, Start/Stop = High Frequency |

The final step in the ADL involves selecting mission profiles for lifetime testing, with the OEM ideally providing operating conditions of the UUT, such as mission profile loading and cooling conditions. According to the guidelines provided in the handbook for robustness validation [35], a mission profile encompasses all relevant operating conditions that an EV drivetrain component may experience throughout its service life. The primary objective of defining a mission profile is to establish accurate load profiles, determine functional limits, identify critical boundary conditions, and specify the necessary simulation and modeling approaches. This process involves systematically defining environmental and operational stressors to effectively assess the lifetime performance of the UUT. In this article, three widely used mission profile datasets are selected based on the discussion with a European OEM, as detailed in Table II.

Through an automation system (i.e., virtual vehicle model), the vehicle mission profile is systematically converted into a corresponding load cycle and seamlessly integrated into the hardware testbed. This automated conversion aims to minimize uncertainties in simulation while significantly reducing the time required for testing. Accurately simulating complex load cycles in accordance with the targeted vehicle model typically demands extensive computational resources and prolonged simulation times. In addition, the automated framework facilitates continuous conversion from mission profile to load cycle specific to the UUT without manual intervention, enhancing testing efficiency.

The LTL Fig. 1(b) utilizes an industry-grade power hardware-in-the-loop (PHIL) system for emulation of the e-motor load for the UUT (i.e., drive inverter). Building on the load profiles generated within the ADL, the LTL replicates real-world operating conditions with high precision, ensuring consistency and reliability in lifetime tests. This PHIL-based setup is designed to be highly adaptable, enabling seamless integration of various mission profile factors, including vibration, temperature fluctuations, and other environmental stressors. By simulating these dynamic external conditions, the LTL provides a comprehensive testing environment that closely mimics real-world automotive scenarios. This approach enhances the predictive accuracy of lifetime assessments and supports the development of robust PECs for automotive applications. To ensure accurate lifetime assessment, several key parameters are measured using high-precision sensors and logged instantaneously at 1 kHz/10 kHz sampling rates. These parameters include phase currents and voltages, modulation index, heatsink and coolant temperatures, flow rate, dc-link voltage and current, as well as load profile data, such as torque, speed, and frequency.

The MML Fig. 1(c) utilizes physics-based digital models to analyze WBG-based UUT, specifically SiC MOSFETs. It employs compact multiphysics models to simplify thermal, electrical, and mechanical interactions of power semiconductors, accurately representing device behavior [36]. Inputs to this layer include geometrical parameters, material data, electrical characteristics, and datasheets of the relevant power device for modeling and numerical simulation, with these models integrating hardware testbed datasets for a comprehensive UUT analysis. The MML addresses key complexities, as follows:

1) coupled multiphysics phenomena, including electromagnetic, thermal, and mechanical interactions;
2) multiscale spatial phenomena, capturing thermomechanical effects from $\mu$m-scale chip interfaces to cm-scale module-level behavior; and
3) temporal dynamics, spanning nanosecond-to-millisecond electrical effects, second-scale thermal responses, minute-scale mission profiles, and lifetime assessments over millions of cycles.

The LAL Fig. 1(d) constitutes the final statistical layer, utilizing temperature data (thermal stress profiles) and die attach damage precursors from the MML as inputs for mission-profile-oriented reliability assessment to assess the lifetime of power semiconductors, specifically SiC MOSFETs, within the UUT under specified mission profiles [11]. Thermal stress profiles are processed via cycle counting algorithms to determine cycles to failure based on temperature variations. Concurrently, mechanical degradation data are integrated to enhance reliability assessments. Statistical models, including Monte Carlo simulations and Weibull distribution fitting, analyze accumulated cycles-to-failure data to estimate component-level lifetimes. Using this data, the overall lifetime of the UUT is calculated by correlating failure probabilities with the SiC MOSFETs, considering the known topology from the ADL. Finally, the output of the LAL is sent back to ADL to establish the DfR loop.

The proposed test-oriented lifetime assessment framework for automotive PECs integrates testing, modeling, and reliability assessment to achieve DfR. Although this study demonstrates the methodology on SiC MOSFET-based PECs, the framework remains adaptable to other semiconductor technologies (e.g., Si and GaN) with appropriate modifications to individual layers. The definitions and interfaces of the layers—ADL, LTL, MML, and LAL—are consistent and applicable, ensuring the framework serves as a generalized solution.

## III. AUTOMOTIVE LIFETIME TESTBENCH

Fig. 2(a) presents an overview of the automotive lifetime test bench. At the core of the test bench is an ALC, comprising ac–dc and dc–ac converters powered by a 3-phase grid. The ac–dc converter serves as a battery emulator, delivering power to the

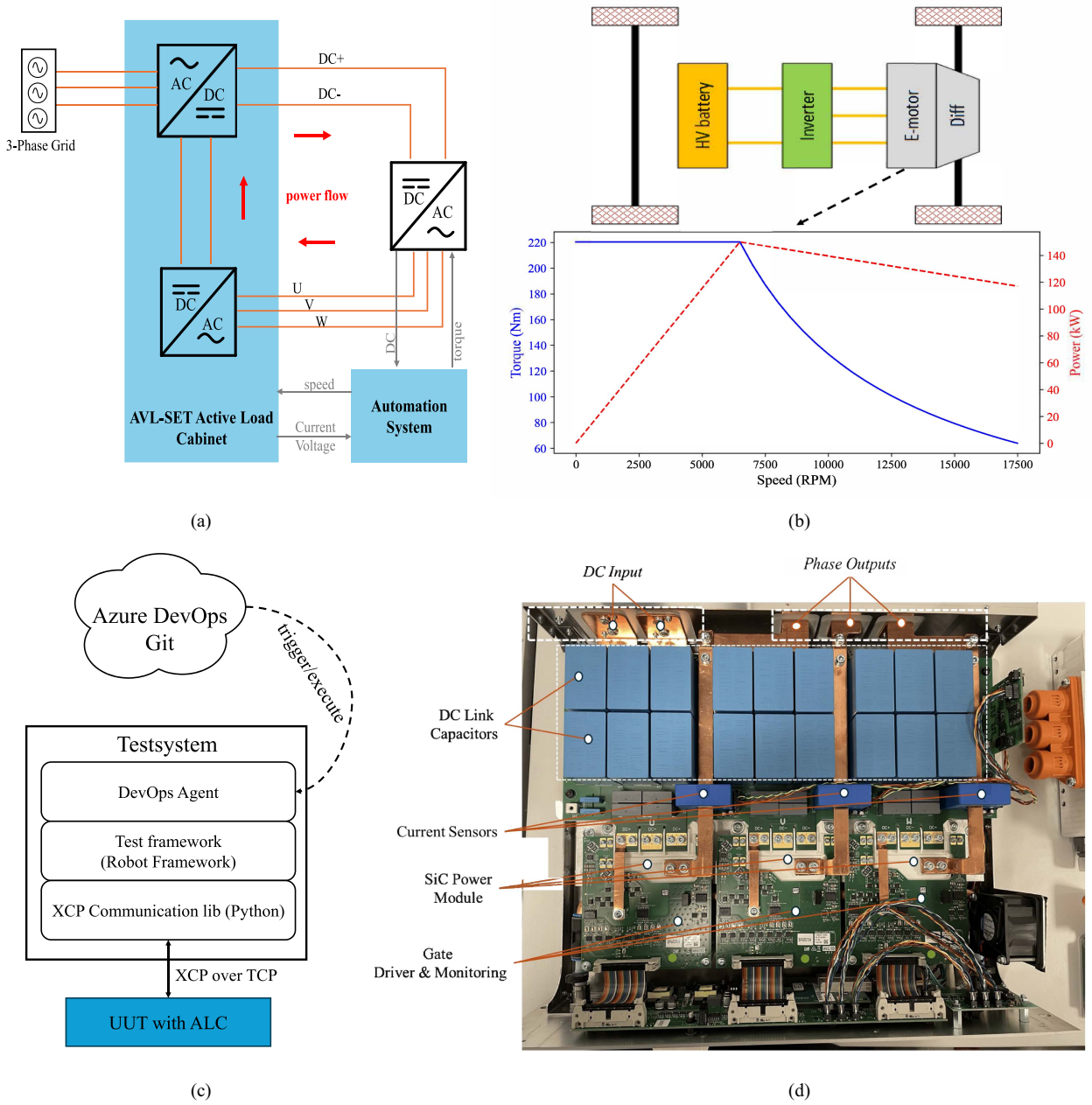


Fig. 2. Automotive lifetime testbench with UUT, active load cabinet and automation system. (a) Test setup of UUT with Active Load Cabinet (ALC) and automation system. (b) Vehicle topology incorporating the UUT (Inverter) and the torque-speed curve of the driven Permanent Magnet Synchronous Motor (PMSM) motor. (c) Automation system with universal measurement and calibration protocol (XCP) communication over transmission control protocol (TCP). (d) UUT 800 V automotive traction inverter hardware.

UUT, while the output of the UUT connects to an ac–dc converter that emulates a passive resistance-inductance load and a linear PMSM. The ALC differs from a traditional E-motor emulator primarily in that the latter provides dc-side galvanic isolation, allowing the ac side to float like that of a real motor, with common-mode voltage determined by parasitic capacitances of the inverter. In contrast, the ALC lacks isolation and instead uses a common-mode choke to manage ac-side common-mode voltage. As a result, the ALC is better suited to steady-state or slowly varying mission profiles, such as WLTP, and offers lower dynamic performance. The ALC supports testing capabilities up to 1000 V dc, 800 Arms, and 500 kW of power. The UUT is an 800 V, 150 kW automotive SiC-based dc–ac power inverter, with its hardware detailed in Fig. 2(d). The inverter is built with a 1200 V MSCSM120AM042CT6LIAG SiC power module rated at 496 A of continuous drain-source current at 25 °C consisting of 6-MOSFET switches in parallel.

The automation system, also depicted in Fig. 2(a), integrates two software tools: AVL VSM and AVL PUMA 2. AVL VSM vehicle simulation model (VSM) is a versatile, real-time simulation software designed to facilitate virtual vehicle development and testing. This test bench simulates various standard driving

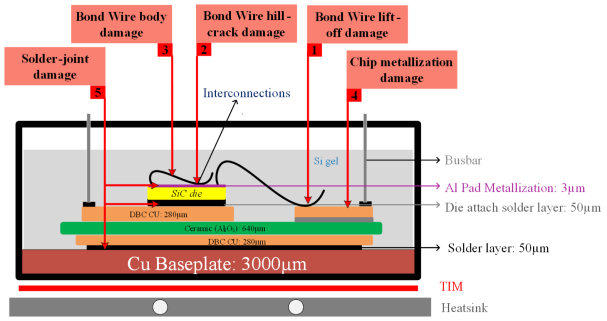


Fig. 3. Cross-sectional view illustrating degradation mechanisms in a SiC power module, including the coefficients of thermal expansion (CTE) for various materials. Red arrows indicate regions within the SiC MOSFETpower module that are susceptible to common failure modes: 1) bond wire lift-off, 2) crack formation in bond wire hills, 3) damage at the bond wire-to-body interface, 4) degradation of chip surface metallization, and 5) solder joint failure.

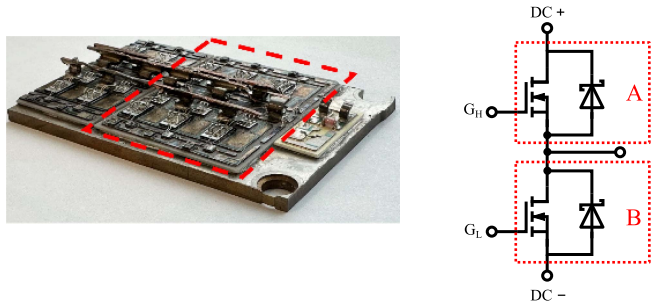


Fig. 4. Real SiC power module specimen. (a) SiC specimen. (b) Half-bridge configuration.

cycles, as outlined in Table II, for an EV. The simulated vehicle has a mass of 2150 kg, features all-wheel drive, and delivers a total engineering power of 450 kW. It is equipped with a wheelbase of 2.7 m and 235/35 ZR20 tires with a radius of 0.325 m. The automation system for testing is smoothly integrated with Azure DevOps, utilizing a connected DevOps agent deployed on the automation machine to facilitate automated testing, prioritizing efficiency, reliability, repeatability, and comprehensive test documentation archiving. The test automation framework incorporates a Python library for XCP over TCP communication with the test system. The DevOps agent is triggered through Azure DevOps to execute tests. The structure of the automation system is depicted in a block diagram in Fig. 2(c). Among the data collected for the three profiles, Fig. 2(b) illustrates the PMSM motor emulation speed and torque during UUT testing for WLTP driving cycle. Complementing this, AVL PUMA 2 is an advanced automation software for test bed control and data acquisition. It is used for recording parameters such as temperatures, currents, voltages, speed, torque, and coolant flow rate at a maximum rate of 1 kHz during the test. The test bench executed experiments across the three profiles listed in Table II, collecting comprehensive data. These data are further used for multiphysics modeling and reliability assessment of the UUT.

## IV. Compact Multiphysics Model

Semiconductor power device failure occurs due to gradual physical degradation accumulated over its operation lifespan in a PEC. Fig. 3 shows a cross-sectional view of a sillicon carbide (SiC) MOSFET, highlighting the main failure mechanism affecting the power module. The most frequent failure modes include solder-joint failure, chip metallization damage, bond wire body damage, bond wire hill cracks, or bond wire lift-off damage. These thermomechanical failures lead to physical deformation from accumulated damage during continuous use [37], [38]. The $T_j$ variation during PEC operation is closely tied to package-level degradation, like bond-wire issues [39]. It is also critical to evaluate mechanical degradation at the chip level, such as solder joint damage at the die attach. This shows the need to consider both the impact of $T_j$ and the permanent mechanical deformation. The inelastic strain indicates the deformations and deteriorations in the material, which accumulate over the thermal cycle and cause permanent mechanical damage to the SiC module, failing the entire PEC. To address this, this section describes the modeling of electrothermal simulation for $T_j$ estimation and the thermomechanical numerical simulation for inelastic strain calculation. The $T_j$ estimation from the electrothermal model is input for the load-based lifetime models (Semikron–Danfoss power cycle test model). This model provides a lifetime without distinguishing between different failure modes (bond wire, die attach). On the other hand, the sequentially coupled electrothermal/thermomechanical simulation provides a detailed analysis of the mechanical stress situation in different regions. In this work, the die attach is analyzed. By use of this approach, an assessment of one specific failure mode (e.g., die attach) can be analyzed.

### A. Electrothermal Model

The electrothermal model consists of two stages, namely loss modeling and a thermal model for $T_j$ estimation. The following subsection describes both models in detail.

*1) Loss Model:* The loss model, encompassing both a conduction loss model and a switching loss model, estimates the instantaneous power losses in all switching devices within the power module during each switching cycle. This model can be easily calibrated using device datasheet information and experimental measurements, facilitating the estimation of conduction and switching losses in both MOSFETs and diodes.

The conduction losses of the SiC-MOSFETs and diodes depend on the instantaneous device currents and voltages, namely the MOSFETdrain-source current ($i_{\mathrm{DS}}$), diode current, MOSFET drain-source voltage, and diode forward voltage. These voltages are influenced by $T_j$ and the corresponding device currents. A typical half-bridge configuration, operated at a phase current $i_{\mathrm{x}}$ and duty cycle $d_{\mathrm{x}}$, is illustrated in Fig. 4(b). Unlike IGBTs, the bidirectional nature of MOSFETs ensures that the current polarity does not impact the conduction paths. Consequently, current flows through either the high-side (HS) or LS MOSFETs, determined by which side receives the turn-ON command. During

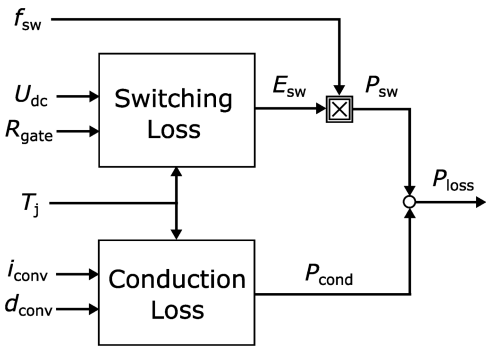


Fig. 5. State block diagram of the loss model.

dead times, current conduction alternates between the MOSFETs and the diodes.

The calculation of half-bridge conduction losses can be summarized as follows:

$$P_{\text{cond}} = \begin{cases} P_{\text{cond,MOS,A}} & \text{if Gate}_A = \text{High, Gate}_B = \text{Low} \\ P_{\text{cond,MOS,B}} & \text{if Gate}_A = \text{Low, Gate}_B = \text{High} \\ P_{\text{cond,Diode,B}} & \text{if Gate}_A = \text{Low, Gate}_B = \text{Low, } i > 0 \\ P_{\text{cond,Diode,A}} & \text{if Gate}_A = \text{Low, Gate}_B = \text{Low, } i < 0. \end{cases} \tag{1}$$

Given the negligible reverse recovery of SiC Schottky diodes, the switching losses are predominantly determined by the turn-ON and turn-OFF components of SiC MOSFETs, $p_{\text{sw,on}}$ and $p_{\text{sw,off}}$. These losses depend on the switching loss energies, $E_{\text{sw,on}}$ and $E_{\text{sw,off}}$, as well as the converter switching frequency, $f_{\text{sw}}$. The values of $E_{\text{sw,on}}$ and $E_{\text{sw,off}}$ can be determined as functions of current, dc-link voltage, and temperature using the data provided in the module datasheet according to the following equation:

$$\begin{aligned} p_{\text{sw}} &= E_{\text{sw,on}}(i_x, T_j, u_{\text{dc}}, R_g) \\ &\quad + E_{\text{sw,off}}(i_x, T_j, u_{\text{dc}}, R_g) \cdot f_{\text{sw}}. \end{aligned} \tag{2}$$

Fig. 5 shows the state block diagram of the loss calculation.

*2) Thermal model:* The thermal model for $T_j$ estimation adopts the methodology outlined in [40] and [41], employing the finite-difference method to spatially discretize the power module into small finite volumes, each with approximately homogeneous material properties and temperature. The initial step involves dividing the three-dimensional geometry of the power module into small cubes, ensuring no internal material transitions occur within each cube. Heat conduction within each cube is modeled using discretized heat transfer equations, with thermal resistances calculated between adjacent elements while considering variations in material properties. The partial differential equation of heat transfer is applied to each cubic element. By integrating the differential equations across all cubes, a state-space model is derived. To accurately define the spatial coordinates, the power module is analyzed using computed tomography (CT) scanning, with the resulting images shown in Fig. 6. The extracted dimensions from this analysis are utilized to determine the coordinates of the cubes and the thickness of the layers within the module stack-up. Fig. 7 depicts the layout of the power module segmented into small cubes.

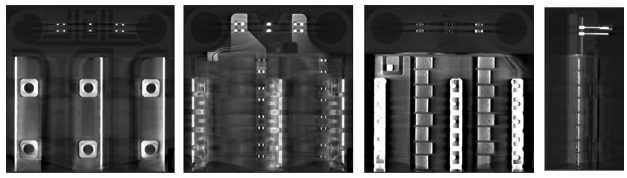

Fig. 6. CT imaging of the power module.

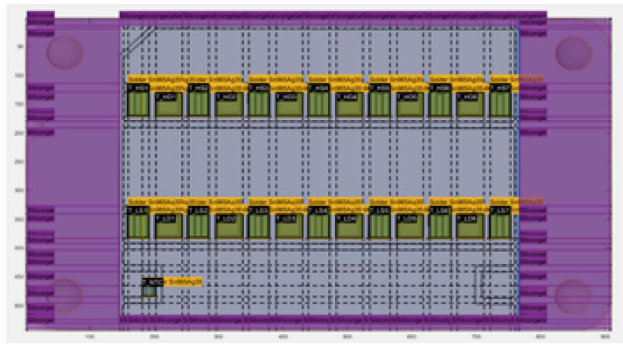

Fig. 7. Layout of the power module.

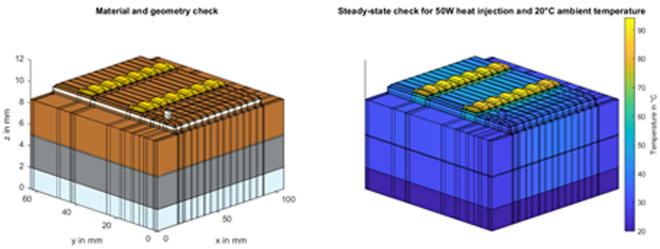


Fig. 8. Steady-state solution of the generated thermal modeling.

Subsequently, the thermal behavior of each cube is represented through a thermal network, incorporating thermal capacitances $C_{\text{th}}^{m,n,p}$ and thermal resistances $R_{\text{th}}^{m,n,p}$ that connect each cube with the coordinates $(m, n, p)$ to its neighboring elements. The differential equations governing all cubes are then consolidated to formulate the state-space thermal model of the power module. This model enables the estimation of transient temperatures at any location within the power module or the computation of steady-state solutions for a given operating point, based on specified initial temperatures and losses, as illustrated in Fig. 8.

Model order reduction is implemented using balanced truncation to enable fast and real-time simulations. This technique reorganizes the system into a balanced realization, ranking states by their energy contribution through Hankel singular values. States with minimal influence are truncated, thereby significantly reducing model complexity while preserving high accuracy. Further details on the modeling strategy and truncation approach are available in [40] and [41].

*3) Model Validation:* The electrothermal model is validated using a dedicated three-phase inverter setup connected to an inductive load, as depicted in Fig. 9(a). This setup includes a dc

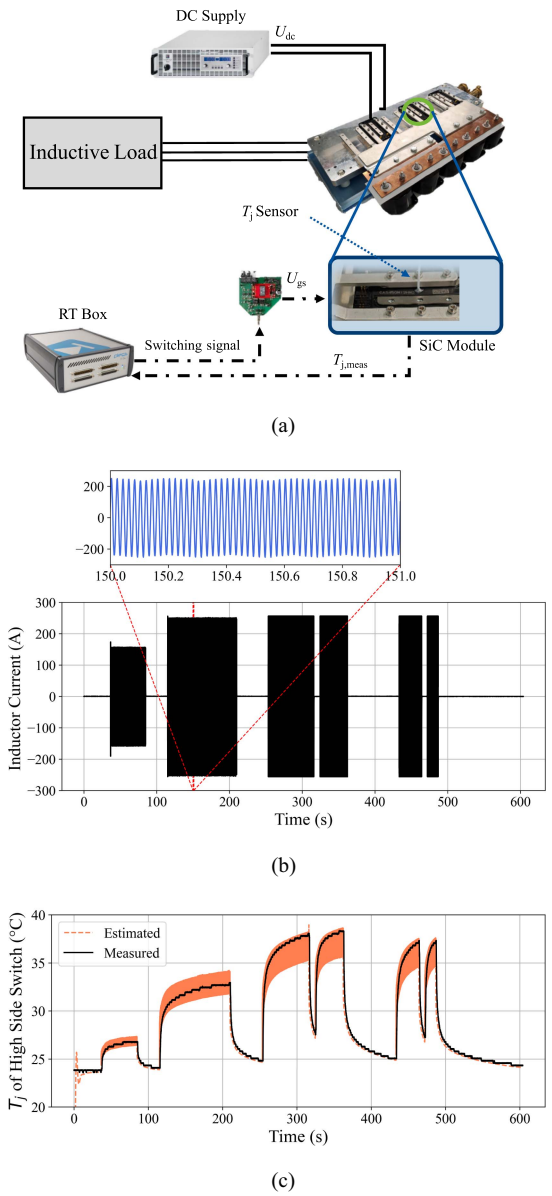


Fig. 9. Process flow for electrothermal model validation. The workflow illustrates the validation test setup, electrical, and thermal characteristics waveforms. (a) Validation test setup for the electrothermal model, utilizing a PLECS RT Box for controlling the inverter operation and to execute the electrothermal model in real time. (b) Applied inductor current to the SiC power module for validation test. The zoomed plot shows the sinusoidal current. (c) Measured and estimated junction temperature ($T_j$) of the SiC MOSFETmodule, showing a mean squared error of 2.2 °C for the central die.

source powering the stand-alone inverter, which is connected to an inductive load composed of three star-connected inductors. The inverter is controlled by a PLECS RT Box serving as the real-time controller. This controller generates gate signals for the gate drivers and records measurement signals from the inverter. The junction temperature, $T_j$, is measured using an optical temperature sensor from Opsens Solutions [42]. During the measurement, the electrothermal model is executed in real time on the RT Box at a sampling rate of 1 kHz to concurrently estimate $T_j$.

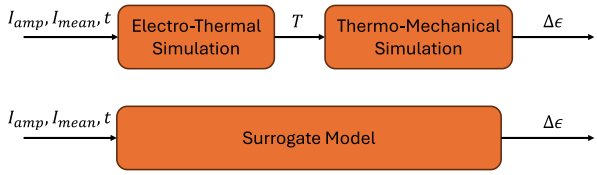


Fig. 10. Coupled electrothermal and thermomechanical model of the PEC for creep strain assessment.

Fig. 9(b) shows the applied inductor current waveform, which is a sinusoidal current with peak values of 150 A and 250 A. The measured and estimated $T_j$ values are presented in Fig. 9(c). As shown, validation against known temperatures yields a mean square error of 2.2 °C for the central HS MOSFET, confirming the accuracy and effectiveness of the developed electrothermal model.

### B. *Sequentially Coupled Electrothermal and Thermomechanical Model*

Wire bond lift-off and die attach failure are two dominant failure modes that can be seen in power modules. Physical active power cycle testing of the power modules is conducted based on the automotive testing standard (AQG 324). The standard describes that a 5% increase in the mosfet forward voltage $(V_f)$ indicate the wire bond lift-off failure mode and 20% increase in the thermal resistance $(R_{\text{th}})$ denotes a die attach failure. The results described in the literature [31] delineate that during the active power cycle test, both failure modes, such as wire bond lift-off and die attach failure have been observed. It has been also noticed from the test that failure criterion based on 5% increase in $V_f$ is achieved, while only very slight increase of $R_{\text{th}}$ is observed. Due to this, relying solely on $R_{\text{th}}$ as an indicator is not sufficient to detect early or partial die attach failures. Accordingly, here the damage in the die attach is not predicted by observing the $R_{\text{th}}$, but by using a physics-based simulation approach.

In this physics-based approach, the creep strain is assessed to calculate the damage in the die attach as its material possess time and temperature-dependent plastic behavior. Creep strain refers to the time-dependent plastic deformation of a material that permanently deforms over time under constant stress, even if the stress is below the material's yield strength. The simulation model for extracting creep strain damage employs a sequentially coupled electrothermal and thermomechanical finite element (FE) approach. Initially, an electrothermal simulation is conducted to find the temperature distribution across the power device. This temperature distribution is then used in the mechanical analysis, as shown in Fig. 10. However, FE simulations are computationally intensive, leading to prolonged execution times that render them impractical for iterative applications. Accurate surrogate modeling based on FE simulations is a widely researched approach to develop fast-executable models [43], whose outputs can be leveraged within test-oriented lifetime assessment frameworks.

Recent research by the authors in [15], [27], and [44] details the FE simulation based on mission profile test data. The numerical simulation considers the active power cycle test based

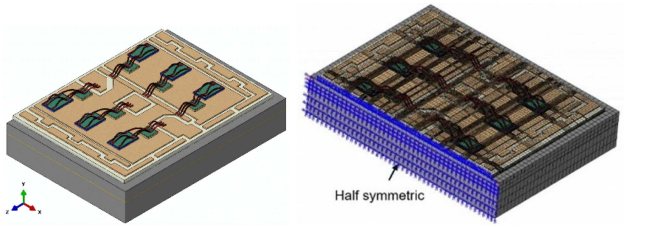


Fig. 11. FE model of the SiC power module. (a) FE model. (b) Mesh and boundary condition.

on the automotive testing standard AQG 324 [45]. The process involves using phase current data and voltage drop from the mission profile test, measured across the chip, to conduct an electrothermal FE simulation. Key details from the phase current data are obtained through the rainflow cycle counting algorithm. This algorithm breaks down the mission profile data into multiple cycles, each defined by a total time ($t$), a mean current ($I_{\text{mean}}$), and a cycle amplitude ($I_{\text{amp}}$). These parameters are fed into the electrothermal FE simulation, which outputs the junction temperature ($T_j$), followed by a mechanical analysis that outputs the strain range ($\Delta\epsilon$). This simulation approach can be linked to the test-based lifetime assessment outlined in Fig. 1, using the developed surrogate model for creep strain calculation with faster computation avoiding the FE analysis.

The SiC MOSFET power module is designed on Abaqus [46] FE analysis software. The SiC specimen is shown in Fig. 4(a), consisting of a direct copper bond substrate where the SiC chip is attached by SAC solder as die attach material. The aluminium wire bonds have a diameter of 300 $\mu$m. A half symmetric model is considered during the numerical simulation for better computational efficiency, as shown in Fig. 11(a). Each layer of the FE model is assigned with corresponding temperature-dependent material properties as in the real sample. The mesh and boundary condition of the FE model is shown in Fig. 11(b).

*1) Electrothermal Simulation:* First, an electrothermal simulation is conducted on the SiC power module to examine the temperature distribution within the system. Each layer is assigned electrical and thermal conductive material properties in the thermal simulation. The electrical conductivity of the SiC chip is sourced from its datasheet. The power module includes an HS and an LS, but only the HS is considered in the thermal analysis. The thermal simulation uses a load current of 240 A with a switching time of $t_{\text{on}}/t_{\text{off}}$ of 3 s/ 3 s, and the results are validated against experimental data. It is observed that the highest junction temperature occurs at the center of the chip, where the active area is located, as shown in Fig. 12(a) and (b). Elevated junction temperatures are noted across all three MOSFET chips. It has been observed from experiment that at the time stamp of 660 s (recorded time) with a current amplitude of 240 A, the $T_j$ of the chip reaches approximately to 130 °C depicted in Fig. 12(c). The maximum junction temperature calculated using FE simulation is 127 °C.

*2) Thermomechanical Simulation:* In the thermomechanical analysis, the temperature obtained from the electrothermal simulation is given as the input load for the mechanical simulation.

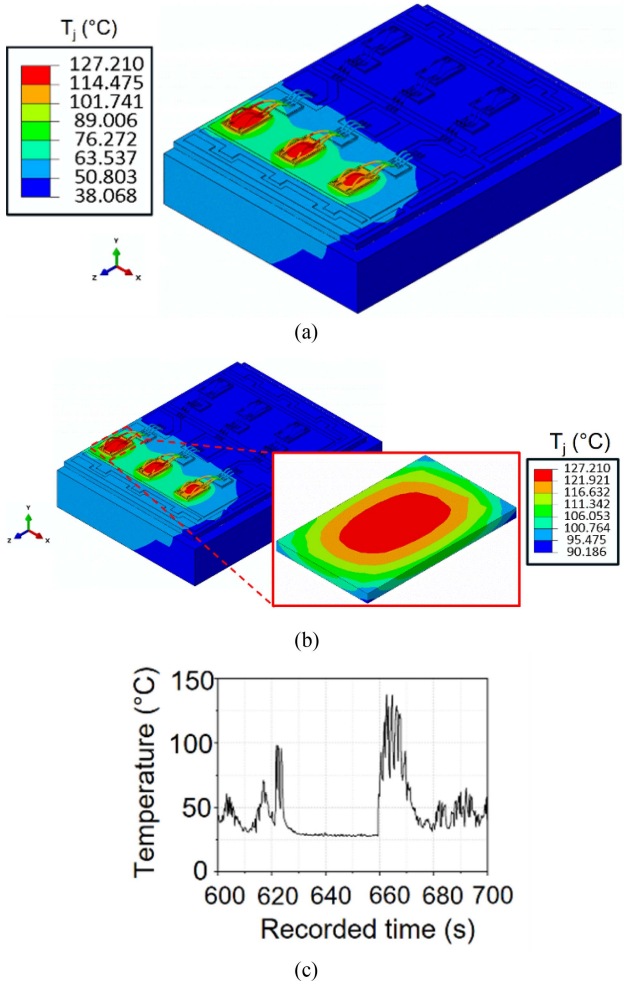


Fig. 12. Temperature distribution of power module from electrothermal FE simulation and experiment. (a) Temperature distribution on the power module. (b) Junction temperature on SiC chip. (c) Temperature profile from experiment.

In mechanical analysis, materials are assigned with temperature-dependent mechanical properties. Creep material property is applied to the die attach material [47]. A thermomechanical analysis was performed for three thermal cycles, and its corresponding stresses and inelastic strains were observed during this investigation. It has been observed that maximum principal stresses on the SiC chip are higher at the end of $t_{\text{on}}$ when compared to stresses at the end of $t_{\text{off}}$ shown in Fig. 13. Higher tensile stress is observed on the chip where the bond wire is located, which is not critical. The accumulation of inelastic strain correlates to the fatigue of materials undergoing elastic or plastic deformations [48]. Since the damage in the die attach should be predicted, the inelastic strain in the die attach is taken into consideration. It is evaluated by means of volume averaging approach to minimize the influence of numerical singularity effect from the numerical simulation [49]. Higher cyclic equivalent creep strain is noticed at the die attach layer's outer periphery, where the material degradation probability is high, as depicted in Fig. 14(a). This implies that the die attach delamination is expected from the corner region toward the centre region of the layer. The grey region in Fig. 14(b) delineates

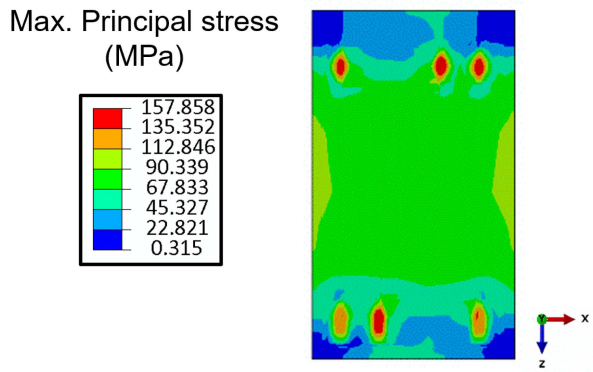


Fig. 13. Maximum principal stresses on SiC chip at the end of $t_{on}$.

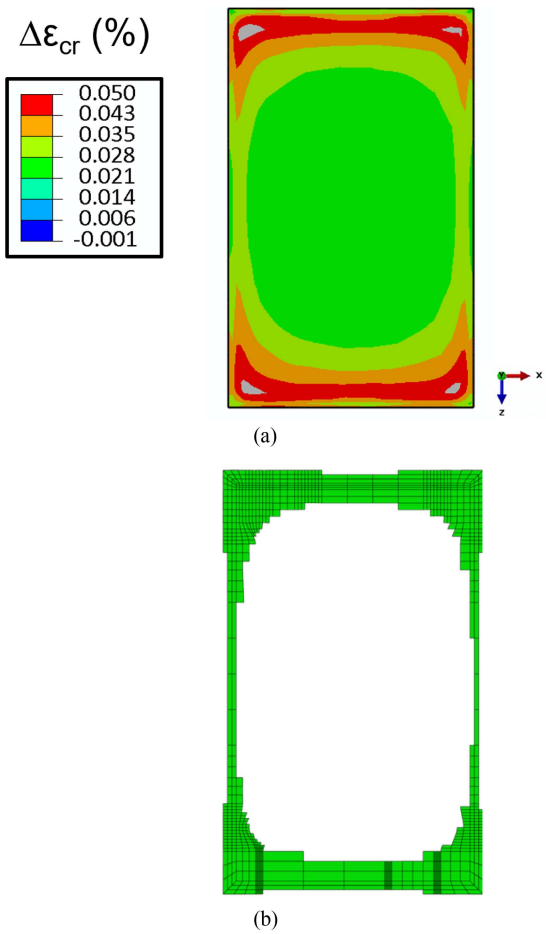


Fig. 14. Cyclic equivalent creep strain in the die attach and its corresponding 10% of elemental volume for averaging. (a) Cyclic equivalent creep strain in the die attach. (b) Elements selected for volume weighted averaging.

that the strain is greater than 0.05%. The averaging method considers 10% of the elemental volume of the die attach layer, which has higher inelastic strain values, and evaluates a discrete weighted averaged inelastic strain value, which will be used for estimating the lifetime based on Coffin–Manson law. The elements considered for the volume weighted averaging are represented in Fig. 14(b).

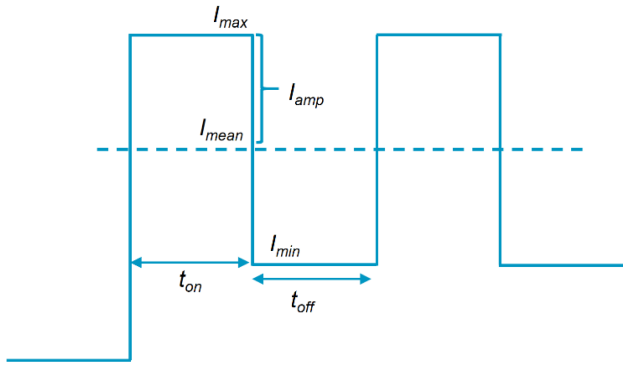


Fig. 15. Current loading profile for electrothermal simulation with switching time.

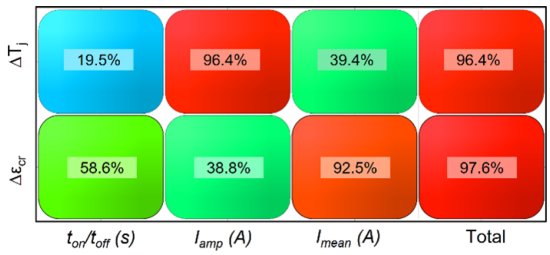


Fig. 16. Coefficient of prognosis matrix.

*3) Development of Surrogate Model:* The surrogate model is designed to use the rainflow cycle counting outputs ($I_{\text{amp}}$, $I_{\text{mean}}$, $t$) as inputs to quickly calculate the resulting creep strain ($\Delta\epsilon$). To determine the ranges for ($I_{\text{amp}}$, $I_{\text{mean}}$, $t$), the current profile of the WLTP is analyzed, and subcycles are extracted. From these subcycles, the ranges of mean current values and cycle amplitudes are used to establish the maximum input ranges for the surrogate model, defined as $I_{\text{amp}} \in (5-250)$ A, $I_{\text{mean}} \in (5-200)$ A, and $t \in (0.1-6)$ s.

A design of experiment is conducted using optiSLang software to cover the entire range of input parameters for the surrogate model. Sixty simulations with varying setups of $I_{\text{amp}}$, $I_{\text{mean}}$, $t_{\text{on}}$, and $t_{\text{off}}$ are performed for three cycles, as shown in Fig. 15. The $t_{\text{on}}$ and $t_{\text{off}}$ are set to half of the total time during the numerical simulation. The surrogate model represents a stabilized cyclic condition, excluding the transient behavior of the cycle. The surrogate model is developed as a metamodel of optimal prognosis (MOP). The MOP provides a simplified representation of a complex model used to predict outputs based on user-defined inputs. The MOP is represented as a response surface. This MOP can be utilized as a surrogate model within the framework by exporting it as an FMU.

The accuracy of output predictions based on given inputs is the critical factor for all surrogate models. The coefficient of optimal prognosis matrix of the model shows how well the MOP's predicted outputs align with the simulated data points relative to the input parameters. The robustness of the surrogate model is determined by the total COP matrix value, which should exceed 90%, as illustrated in Fig. 16 for the developed surrogate model. The total COP value surpasses 95%. The COP

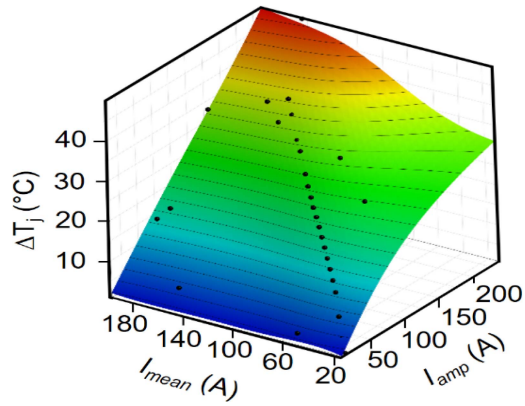


Fig. 17. Response surface of $\Delta T_j$ on the chip based on $I_{\text{mean}}$ and $I_{\text{amp}}$.

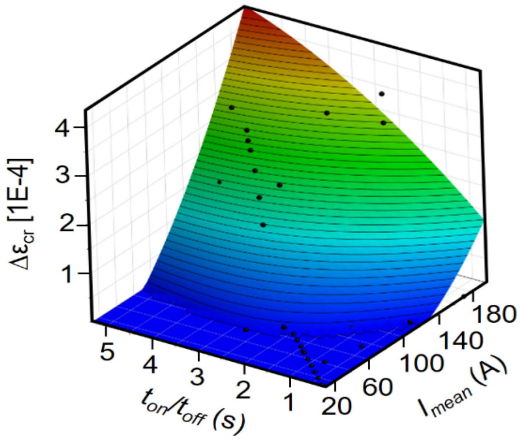


Fig. 18. Response surface of cyclic equivalent creep strain in the die attach with respect to $I_{\text{mean}}$ and $t$.

matrix also quantitatively indicates the influence of each input parameter on the output results. Fig. 16 shows that $I_{\text{amp}}$ has a greater impact on the junction temperature difference, while the cyclic equivalent creep strain is more significantly affected by $I_{\text{mean}}$. The switching time ($t_{\text{on}}/t_{\text{off}}$) also contributes to the accumulation of $\Delta\epsilon_{\text{cr}}$. The MOP presents information as a 3-D response surface, depicting the output responses as functions of the input parameters. These response surfaces are plotted based on the most influential parameters identified from the COP matrix. Fig. 17 shows that as the current amplitude ($I_{\text{amp}}$) and mean current ($I_{\text{mean}}$) increase, the temperature difference across the chip also rises. The thermal resistance of the power electronic system increases with higher current amplitude, resulting in greater temperature dissipation on the chip. The mean current ($I_{\text{mean}}$) and switching time ($t_{\text{on}}/t_{\text{off}}$) significantly affect the cyclic equivalent creep strain accumulation in the die attach. Thus, the output response surface of $\Delta\epsilon_{\text{cr}}$ as a function of $I_{\text{mean}}$ and $t_{\text{on}}/t_{\text{off}}$ is shown in Fig. 18. It is observed that larger switching times and higher $I_{\text{mean}}$ lead to greater creep strain accumulation in the die attach, which is also associated with an increased temperature difference across the chip (see Fig. 17). The discrete creep strain values are utilized to estimate the lifetime based on

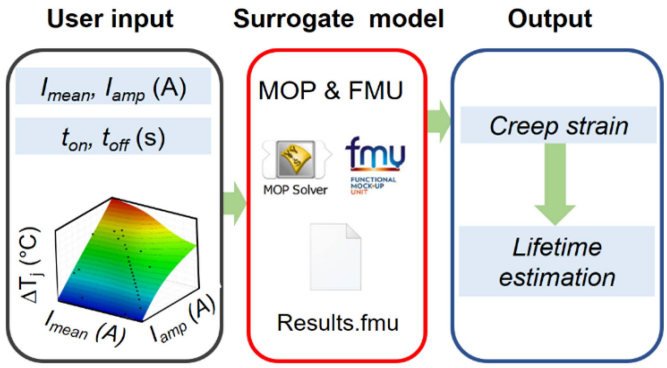


Fig. 19. Block diagram for the application of surrogate model.

the Coffin–Manson law. A generic model has been developed using this metamodel in the form of an FMU.

The surrogate model is applicable for the lifetime assessment of the power module without any further FE simulations. The main advantages of these models are the simulation times can be reduced and also able to predicts the lifetime with different inputs within short period of time. Fig. 19 shows the workflow of the surrogate model during the lifetime assessment. The end user can easily define their input parameters in the user input section and surrogate model section will evaluate the creep strain as the output parameter and at output section the lifetime of the module can be estimated. The developed FMU can be accessed by using different programming languages, such as Python, MATLAB, C, and C++.

## V. Combined Lifetime Assessment Model

Standard accelerated lifetime tests, including power cycling ($\text{PC}_{\text{sec}}$, $\text{PC}_{\text{min}}$) and thermo-shock tests, are performed on power modules under varying load conditions (temperature amplitude, load current) to determine the number of cycles to failure. Corresponding FE simulations of the power module are conducted to evaluate the mechanical stresses in critical regions, such as the bond-wire, die attach, and metallization. These regions are further examined through physical failure analysis techniques, including scanning acoustic microscopy, cross-sectioning, and X-ray CT, enabling correlation between measured mechanical stress, damage contribution, and associated failure modes.

The proposed lifetime assessment model integrates damage contributions from two primary degradation mechanisms in SiC-based inverters, as detailed in Section IV. Bond-wire degradation is attributed to electrothermal damage driven by electrical power loss and junction-temperature ($T_j$) cycling. Die-attach degradation is assessed from electro-thermomechanical stresses. The combined model aggregates both mechanisms and applies statistical analysis to estimate system-level lifetime as the probability of failure over operating years or mileage (vehicle usage).

A step-by-step overview of this combined lifetime assessment model is presented in Fig. 20. This section provides a detailed, step-by-step description of the combined lifetime assessment model. Referring to Table II, this section presents data and graphs for the WLTP cycle data, unless otherwise specified. The

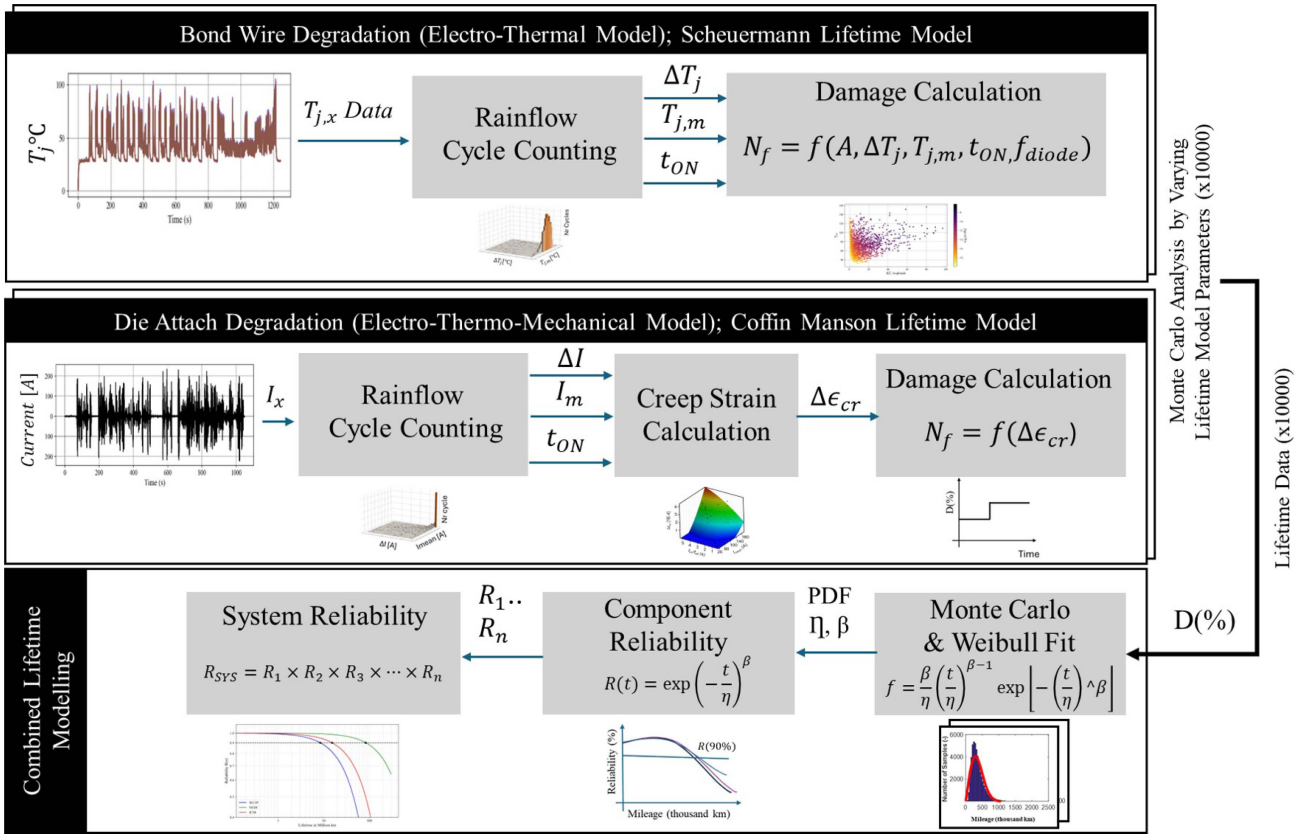


Fig. 20. Overview of combined lifetime assessment model showcasing the full workflow and integration of electrothermal damage and electro-thermomechanical damage calculation to obtain system-level lifetime.

methodology remains consistent for all mission profiles listed in Table II and the composite mission profile described in later sections.

### A. Input to Combined Lifetime Assessment Model

The lifetime assessment model utilizes two primary input datasets: the $T_j$ of six switches assembly and six diodes assembly within the inverter, derived from electrothermal simulation, and root mean square (rms) current for each phase (U, V, W) of the inverter. The phase current data are acquired from the test bench, detailed in Section III, during mission profile testing. These test bench data are subsequently processed using the multiphysics model and electrothermal simulation, described in Section IV, to generate the $T_j$ data. The $T_j$ data are available only for a single SiC module (one leg) of the inverter, encompassing the HS switch-and-diode assembly (HS, HD) and the LS switch-and-diode assembly (LS, LD). Each switch or diode assembly within the SiC power module comprises six switches and diodes connected in parallel. For system-level lifetime assessment, it is assumed that the $T_j$ of the other two legs of the inverter matches the available data from the single leg. Fig. 21 illustrates the $T_j$ for the HS switch for the WLTP profile, displaying the temperature of all six parallel switches. A mean temperature is calculated from these six $T_j$ values for subsequent processing. In addition, the rms current for phase U for the WLTP profile is presented in

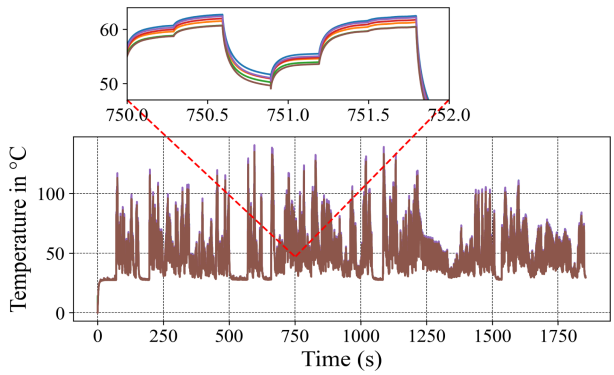


Fig. 21. HS switch $T_j$ data for WLTP mission profile. Similar data are available for LS switch, HS switch, and HS diode for WLTP, NEDC, JC08.

Fig. 22. Both datasets—the $T_j$ and rms current—are available for all mission profiles and are used in further analysis.

### B. Rainflow Cycle Counting Algorithm

To analyze the fatigue or degradation occurring when a system is subjected to stress or strain, a cycle counting algorithm is necessary to identify and quantify the periodic loading or hysteresis stress loops a material has gone through, along with the amplitude and mean of these cycles [50]. The algorithm used for

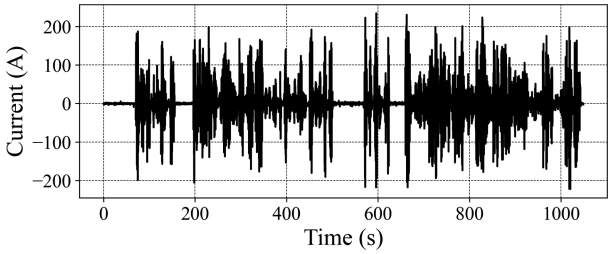


Fig. 22. Phase U rms current for WLTP mission profile. Similar data are available for phase V, and W for WLTP, NEDC, JC08.

such analysis belongs to the class of cycle counting algorithms, with the rainflow counting algorithm (RCA) being the most popular and widely accepted among them. As the rainflow cycle counting algorithm is standardized in ASTM E1049-85 (standard practices for cycle counting in fatigue analysis) [51], this article does not delve into the details of its implementation but instead focuses on the output it provides and the significance of that output.

The RCA provides three key outputs: the amplitude and mean of the loading cycle, and the counted number of cycles, either 0.5 (half cycle) or 1 (full cycle). In the context of the current work, the algorithm processes two inputs: the $T_j$ and the phase current. For the given time-series input such as $T_j$ or I, the algorithm computes the following output.

1) *Amplitude:* $\Delta T_{ji}$ or $\Delta I_i = \frac{S_{\max,i} - S_{\min,i}}{2}$, where $S_{\max,i}$ and $S_{\min,i}$ are the maximum and minimum values of the i-th extracted cycle.
2) *Mean*: $T_{jmi}$ or $I_{im} = \frac{S_{\max,i} + S_{\min,i}}{2}$, showing average stress level of the $i$th cycle.
3) *Number of cycle($n_i$)*: $n_i = 1$ for full cycle and $n_i = 0.5$ representing half cycle as standardized in ASTM E1049-85.
4) *Ton*: Time duration of the hysteresis cycle.

A script is used to bin the amplitude and mean outputs and calculate the number of cycles occurring within each bin to visualize the output of the RCA. Fig. 23 illustrates the three-dimensional histogram data after binning.

### C. Lifetime Assessment for Eletrothermal Damage

The electrothermal damage is assessed by analysing the fluctuation of $T_j$ of the power switch or diode. The output of the RCA for $T_j$, that is, $(\Delta T_j, T_{jm}, n_i, t_{on})$ is provided as an input to the lifetime model equation to compute the individual lifetime of MOSFETs and diodes. In this article, the parametric lifetime model is adopted from the latest Semikron–Danfoss power cycling test model [52]. The model is outlined in (3), and the values of the corresponding parameters are presented in Table III. The model is built upon the well-established Arrhenius and Coffin–Manson model [29], also popularly known as the Scheurmann model

$$N_f = A \times (\Delta T_j)^{\alpha} \times (\text{ar})^{\beta_1 \cdot \Delta T_j + \beta_0} \times \left[\frac{C + (t_{\text{ON}})^{\gamma}}{C+1}\right] \times e^{\left(\frac{E_a}{k_b \times T_{jm}}\right)} \times f_{\text{diode}}. \quad (3)$$

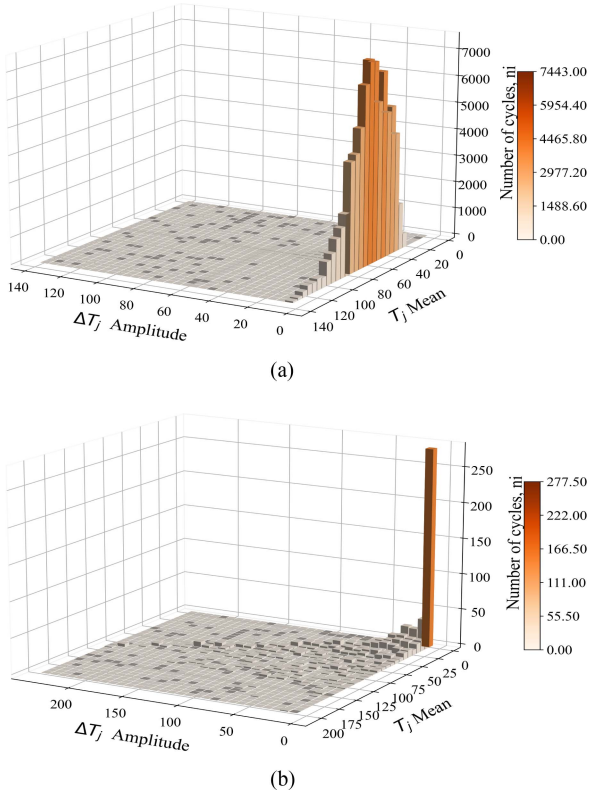


Fig. 23. Rainflow cycle counting algorithm output. Similar data are available for all $T_j$ and I data for all mission profiles. (a) Cycle counting data for HS switch $T_j$ for WLTP Cycle. (b) Cycle counting data for phase current $I_U$ for WLTP Cycle.

TABLE III
PARAMETERS AND THEIR VALUES WITH CORRESPONDING TESTING CONDITIONS

| Parameter | Unit | Value | Testing condition |
|---|---|---|---|
| $A$ | [−] | $3.4368 \times 10^{14}$ | − |
| $\alpha$ | [−] | $-4.983$ | $64\,\text{K} \leq \Delta T_j \leq 113\,\text{K}$ |
| $\beta_1$ | [−] | $-9.012 \times 10^{-3}$ | $0.19 \leq \text{ar} \leq 0.42$ |
| $\beta_0$ | [−] | $-1.942$ | $0.19 \leq \text{ar} \leq 0.42$ |
| $C$ | [−] | 1.434 | $0.07\,\text{s} \leq t_{\text{ON}} \leq 63\,\text{s}$ |
| $\gamma$ | [−] | $-1.208$ | − |
| $f_{\text{diode}}$ | [−] | 0.6204 | − |
| $\alpha_r$ | [−] | 0.31 | − |
| $E_a$ | [eV] | 0.06606 | $32.5°\text{C} \leq T_{jm} \leq 122°\text{C}$ |
| $k_b$ | [eV/K] | $8.61733 \times 10^{-5}$ | − |
| $L_f$ | [h] | 5,000 | @ 85°C |
| $T_f$ | [K] | 358 | − |
| $V_f$ | [V] | 1200 | DC |

The lifetime model in (3) produces $N_f$, which indicates the number of cycles to failure based on a specific set of rainflow counting output $(\Delta T_j, T_{jm}, n_i, t_{\text{on}})$. The developed software supports user-defined parameters and various equation-based models as long as they produce $N_f$ using a similar set of input and parameters as (3). Degradation for this set of counted cycle is $n_i/N_f$. Fig. 24 illustrates the calculated damage $(n_i/N_f)$ as a function of $T_{j,m}$ and $\Delta T_j$. Higher damage is observed for larger $\Delta T_j$ and elevated $T_{j,m}$. The total damage accumulation across the entire $T_j$ profile is determined using Miner's rule, expressed

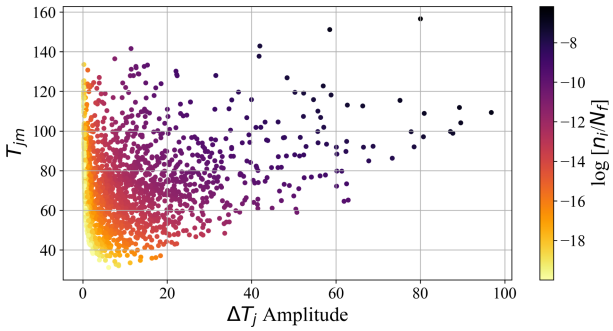


Fig. 24. Plot of degradation $(n_i/N_f)$ for the HS component, derived from rainflow cycle counting of $T_j$ data under the WLTP driving cycle.

as given in the following equation:

$$LC_1 = \sum_{i=1}^{k} \frac{n_i}{(N_f)_i}. \tag{4}$$

The lifetime of an individual MOSFET or diode is calculated by leveraging the condition that $LC_1$ reaches 1 at failure. The total operational seconds (OPS) are derived from (5), $T_{\text{end}}$ representing the mission profile's total duration. Similarly, operating years are calculated using (6), where $h \in (0, 1)$ acts as a factor that adjusts for the daily operational fraction of the UUT, facilitating normalization and comparison across mission profiles of different time lengths through scaling with $h$ . In addition, the operational lifetime can also be expressed in terms of the total distance covered before the end of life, based on the vehicle's average speed during operation, which is taken as 20 km/h in this study

$$\text{OPS} = \frac{T_{\text{end}}}{LC_1} \tag{5}$$

$$\text{OPY} = \frac{\text{OPS}}{365 \times 3600 \times h}. \tag{6}$$

The OPY is calculated for each mission profile in Table II and for each switch and diode, specifically HS, LS, HD, and LD, to determine the individual operating lifetime based on the corresponding $T_j$ profile.

### D. Lifetime Assessment for Eletro-Thermomechanical Damage

As outlined in Section IV, the RCA based on temperature for load-based lifetime models helps to analyze the mission profile to quantify fatigue cycles. In this research, RCA based on current profile for sequentially coupled electrothermal/thermomechanical simulation-based lifetime models is used for estimating the number of cycles with respect to load current and time. Due to the linear damage model, the order of load cycles do not have any impact on the derived damage—higher order damage models (nonlinear) would be necessary to take the order into account. The RCA output from the phase current, including total time $(t)$, mean current $(I_{\text{mean}})$, and cycle amplitude $(I_{\text{amp}})$, is fed into the developed FMU to calculate inelastic creep strain damage $(\Delta\epsilon_{\text{cr}})$. The surrogate model, implemented as an FMU, can produce $\Delta\epsilon_{\text{cr}}$ without requiring additional FE simulations. Equation (7) describes the Coffin–Manson model used to determine the number of cycles to failure $(N_f)$ based on a given $\Delta\epsilon_{\text{cr}}$. The parameter values for the equation are $C_1 = 0.055$ and $C_2 = 2.3$ [53]

$$N_f = C_1 \times (\Delta\epsilon_{\text{cr}})^{-C2}. \tag{7}$$

The accumulated damage can be calculated using Palmgren-Miner Damage accumulation rule, similarly to 4, as given in 8, where $n_i$ is the number of cycles for the set of $(I_{\text{amp}}, I_{\text{mean}}, t)$, and $LC_2$ denotes the accumulate damaged on the entire phase current profile. It assumes a linear accumulation of damage for each cycle. In reality we see a nonlinear behavior, specifically $V_f$ od $R_{\text{th}}$ under power cycle test condition. Progressive damage behavior is not considered at the current state

$$LC_2 = \sum_{i=1}^{k} \frac{n_i}{(N_f)_i}. \tag{8}$$

Likewise, $LC_2$ is applied in (5) and (6) to compute the OPS and OPY for the three switches associated with the currents IU, IV, and IW for each mission profile.

### E. Monte Carlo Simulation and Weibull Fit

The inherent uncertainty in semiconductor device manufacturing and the packaging process is reflected in the variation of the parameters of the life-time model. So it becomes necessary to analyse how the variation of the parameter of the lifetime model described in (3) and (7) impacts the calculated lifetime of each component namely HS, LS, HD, LD, and from phase current data IU, IV, and IW. As there is no standard data available on the variation of the lifetime model parameters, a random dataset with normal distribution is generated with variation of the parameter from the value given in Table III, corresponding to a standard deviation scaling factor of 0.04. The parameters $A, \alpha, ar, \beta_1, \beta_0, C, \gamma, E_a, f, n, V_f, T_f, L_f$ in (3) and $C_1, C_2$ in (7) is varied for Monte Carlo analysis according to (9), where $P$: Normal distribution dataset, $p$: parameter, and $\mathcal{N}$: Denotes the normal distribution with stdVar: 0.04

$$P = p[1 + \text{stdVar} \times \mathcal{N}(0, 1)]. \tag{9}$$

By using the above parameter dataset and lifetime equations described in Sections V-C and V-D, the range of resulting lifetime is evaluated in terms of distance covered before end of life in million kilometres. The resulting dataset is a distributed lifetime dataset. In this study, 10 000 simulation runs are performed, resulting in the lifetime dataset for each component, namely HS, LS, HD, LD, and phase current data IU, IV, and IW. The resulting random dataset from the Monte Carlo analysis is fit using the Weibull distribution, whose probability density function (PDF) is expressed in (10), where $\beta$ is the shape parameter, $\eta$ is the scale parameter, and $t$ is the lifetime duration in million km. The resulting data of the Monte Carlo analysis and the corresponding Weibull fit are shown in Fig. 25 for the HS and LS switch and

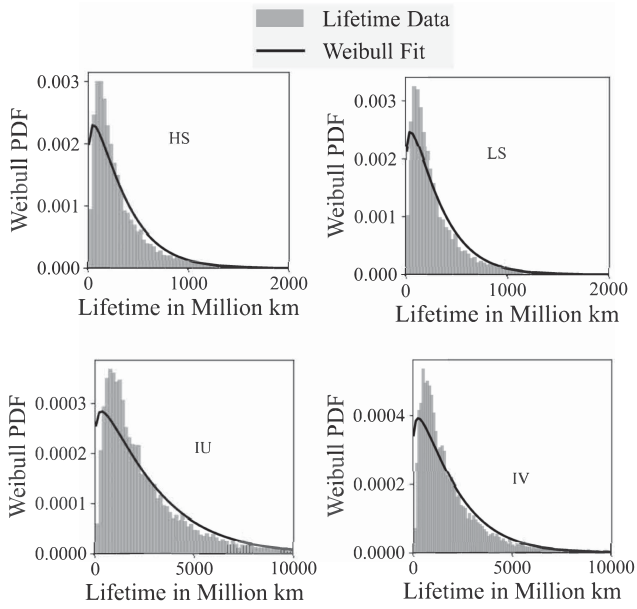


Fig. 25. Monte Carlo lifetime distribution derived from 10 000 simulations, applying a standard deviation scaling factor of 0.04 to the lifetime model parameters for the HS and LS switches, using phase current data from IU and IV under the WLTP driving profile. The results are presented in a histogram overlaid with the corresponding Weibull PDF.

lifetime derived from the phase current of IU and IV phase for the WLTP cycle. Similar data are available for all other mission profile data as well

$$f(t;\beta,\eta) = \frac{\beta}{\eta}\left(\frac{t}{\eta}\right)^{\beta-1} \exp\left(-\left(\frac{t}{\eta}\right)^{\beta}\right), \quad t \geq 0. \tag{10}$$

### F. System Level Reliability Analysis

Reliability of each component needs to be evaluated to calculate the system-level lifetime from the Weibull PDF data. In the Weibull fit, the parameter $\beta < 1$ suggests the failure to be due to factory defect, while $\beta > 1$ suggests failure due to continuous wearout during component operation, and parameter $\eta$ indicates the time when 63.2% of the population is expected to fail. Thus, the reliability function for the Weibull distribution is given in the following equation:

$$R(t;\beta,\eta) = \exp\left(-\frac{t}{\eta}\right)^{\beta}. \tag{11}$$

Using the above equation, reliability data for each of the mission profile data, i.e., $T_j$ for HS, LS, HD, LD, and phase current data for IU, IV, IW phases, is evaluated. The resulting reliability data are denoted as $R_{\text{HS}}$, $R_{\text{LS}}$, $R_{\text{HD}}$, $R_{\text{LD}}$, $R_{\text{IU}}$, $R_{\text{IV}}$, and $R_{\text{IW}}$. All the data for the WLTP mission profile is illustrated in Fig. 26, which also shows the zoomed area for 99% reliability. It can be seen that the reliability from the $T_j$ profile of LD and HD cannot be accessed, as they exhibit significantly less accumulated degradation compared to other data.

The system-level reliability is determined through a series of failures association of all individual reliabilities, achieved by

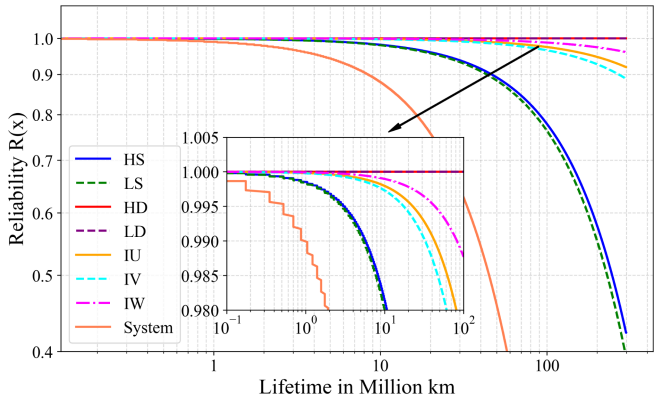


Fig. 26. Lifetime estimation results for individual components (i.e., HS, LS, HD, LD), phase current data for phases IU, IV, IW, and the overall inverter system under the WLTP profile. The zoomed-in region highlights reliability estimates up to 98%.

multiplying them, as presented in the following equation:

$$R_{\text{SYS}}(t) = R_1 \times R_2 \times R_3 \times \ldots\ldots\ldots R_n \text{ for } t \geq 0. \tag{12}$$

In the context of this study, the system comprises three HS switches/diodes, three LS switches/diodes, and a 2-SiC power module influenced by the phase current affecting both high and LSs. The final equation employed for system-level reliability evaluation is given in the following equation:

$$R(t)_{\text{SYS}} = R(t)^3_{\text{HS}} \times R(t)^3_{\text{LS}} \times R(t)^3_{\text{LD}} \times R(t)^3_{\text{HD}} \times R(t)^2_{\text{IU}} \times R(t)^2_{\text{IV}} \times R(t)^2_{\text{IW}} \quad \text{for } t \geq 0. \tag{13}$$

Using the above equation, the system reliability is calculated. Fig. 26 also shows the system-level reliability calculated for WLTP cycle from (13).

This section provided a complete overview of the combined lifetime assessment model developed with WLTP cycle data as reference. The following section details various analyses and results for all three mission profiles using the developed model.

## VI. Mission Profile-Based Lifetime Assessment

The previous section outlined the overall structure of the lifetime assessment model using the WLTP cycle as a representative example. In the experimental test bench, lifetime tests were conducted for three standard driving profiles: WLTP, NEDC, and JC08, as summarized in Table II. This section presents a detailed comparison of these profiles, along with the corresponding results from the lifetime assessment model. Key findings and insights derived from the comparative analysis are also discussed.

### A. Mission Profile Assessment

Fig. 27 illustrates the requested motor speed trajectories for the WLTP, NEDC, and JC08 driving profiles. To enable a deeper analysis, the corresponding motor acceleration profiles, derived from the speed data, are shown in Fig. 28.

Based on a visual analysis of the acceleration graph, a benchmark of $\pm 4000$ r/min/s is established to calculate the number of acceleration and deceleration events for each profile. The

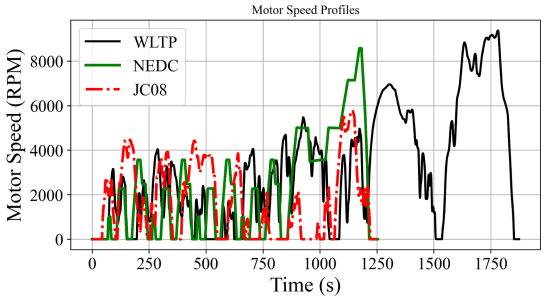


Fig. 27. Speed of the motor in RPM for all three mission profiles (red—JC08, green—NEDC, and black—WLTP).

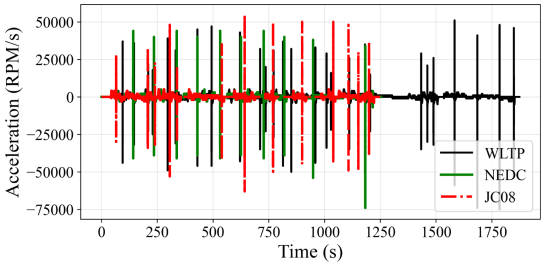


Fig. 28. Benchmark of motor acceleration in RPM for all three mission profiles (red—JC08, green—NEDC, and black—WLTP).

TABLE IV
ESTIMATED COMPONENT AND SYSTEM LIFETIMES AT 99% AND 90% RELIABILITY PERCENTILE (IN MILLION KILOMETERS) AND RELIABILITY PERCENTILE AT 480 THOUSAND KMS

| Profile | HS | LS | IU | IV | IW | System |
|---|---|---|---|---|---|---|
| **99% Reliability (in M kms)** | | | | | | |
| WLTP | 5.8 | 5.4 | 43.1 | 32.7 | 82.7 | 0.96 |
| NEDC | 103.2 | 108.1 | 88.8 | 91.8 | 75.0 | 10.3 |
| JC08 | 11.4 | 10.5 | 55.5 | 33.3 | 45.5 | 1.75 |
| **90% Reliability (in M kms)** | | | | | | |
| WLTP | 46.6 | 43.4 | – | 269.4 | – | 8.4 |
| NEDC | – | – | – | – | – | 83.6 |
| JC08 | 95.5 | 88.1 | – | 262.8 | – | 15.2 |
| **Reliability Percentile (in 480 thousand kms)** | | | | | | |
| WLTP | – | – | – | – | – | 99.5417 |
| NEDC | – | – | – | – | – | 99.9647 |
| JC08 | – | – | – | – | – | 99.7491 |

number of acceleration events recorded for WLTP, NEDC, and JC08 was 1640, 42, and 810, respectively, while deceleration events totaled 3315, 577, and 201. These data reveal that the WLTP cycle is the most dynamic and demanding, characterized by frequent transients, whereas the NEDC cycle predominantly features steady-state operation. Given the direct relationship between load transients and thermal cycling stress, it is expected that the WLTP cycle will induce faster degradation, resulting in the shortest lifetime. In contrast, the NEDC profile, due to its lower dynamic content, is anticipated to yield the longest lifetime considering the same compact modeling framework.

### B. Impact of Mission Profile on Lifetime

The mission profile exerts a substantial influence on the estimated lifetime of power semiconductor components and the overall PEC system. Table IV presents the estimated lifetimes at 99% and 90% reliability levels (in million kilometers) for individual components—including HS and LS switches, as well as phase current paths (IU, IV, IW)—under three standard driving profiles: WLTP, NEDC, and JC08. In addition, the table depicts the corresponding system-level reliability values at 480 000 km (i.e., automotive target service life) A comparison of the mission profiles is illustrated in Fig. 29, with reliability R(x) plotted as a function of lifetime in million kilometers in Fig. 29a, and a system-level lifetime bar graph comparing the different mission profiles at 90% and 99% reliability in Fig. 29b.

Notably, the WLTP cycle, characterized by aggressive transient behavior and frequent acceleration–deceleration events, leads to significantly accelerated aging. For example, at the 99% reliability level, the HS and LS switches under WLTP exhibit lifetimes of only 5.8 Million km and 5.4 million km, respectively, compared to more than 100 million km under NEDC. This nearly 20-fold disparity underscores the strong correlation between thermal cycling severity and mission-induced stress levels.

At the system level, the lifetime under WLTP is only 0.96 million km at 99% reliability—drastically lower than NEDC (10.3 million km) and JC08 (1.75 million km). Even at the 90% reliability level, WLTP achieves just 8.4 Million km, while NEDC supports more than 83.6 million km. Furthermore, reliability percentiles at a fixed distance of 480 000 km confirm this trend: WLTP yields 99.54% system reliability, compared to 99.96% for NEDC and 99.75% for JC08.

These results highlight the critical limitations of generalized, worst-case load assumptions and affirm the need for mission-profile-specific reliability modeling. Accurate lifetime analysis must be grounded in real-world operational data to fully capture the nonlinear degradation dynamics induced by diverse driving conditions.

### C. Impact of Multidomain on Component and System-Level Lifetime

As indicated in Table I, the procedure to integrate both electrothermal (bond wire degradation) and electro-thermomechanical (die attach degradation) represents a distinctive feature of the developed combined lifetime assessment model. A comparative analysis is also required to evaluate the extent to which the overall system lifetime is influenced by various mission profile data, namely $T_j$ of HS, LS, HD, LD, and electro-thermomechanical damage from phase current IU, IV, IW. To this end, the system-level reliability (13) is adapted to compute the contribution of each term through logarithmic addition, followed by calculating the percentage contribution, as demonstrated in (14) for the HS component. The contributions of other reliability terms can be determined similarly

$$\begin{aligned}\text{Total} = {} & |3\log(R(t)_{\text{HS}})| + |3\log(R(t)_{\text{LS}})| \\ & + |3\log(R(t)_{\text{LD}})| + |3\log(R(t)_{\text{HD}})| \\ & + |\log(R(t)_{\text{IU}})| + |2\log(R(t)_{\text{IV}})| \\ & + |2\log(R(t)_{\text{IW}})|\end{aligned}$$

$$\text{Contribution}_{\text{HS}} = \frac{|3\log(R(t)_{\text{HS}})|}{\text{Total}} \times 100. \tag{14}$$

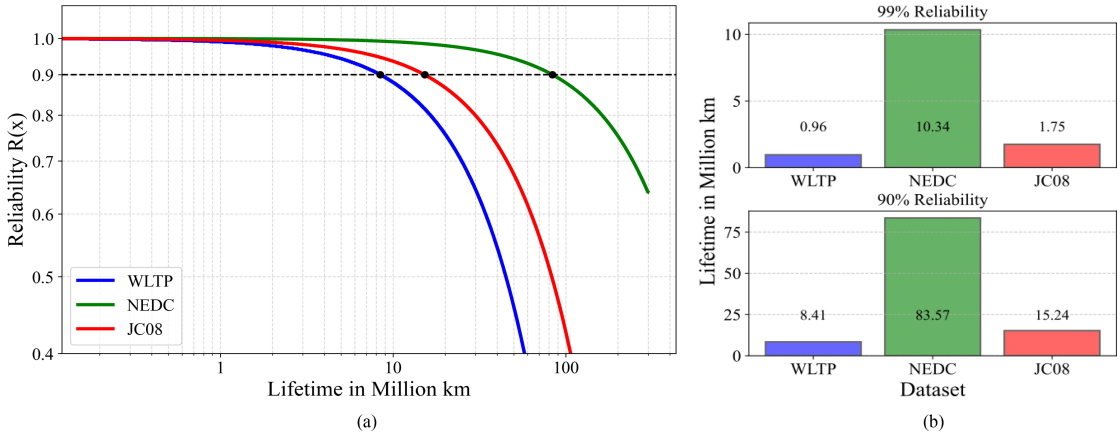


Fig. 29. Reliability-based lifetime estimation of the inverter system UUT under three standard driving profiles: WLTP, NEDC, and JC08. (a) Lifetime estimation of the inverter system UUT as a function of vehicle mileage (in million kilometers) for WLTP, NEDC, and JC08 driving profiles. (b) Estimated lifetimes (in million kilometers) at 99% and 90% reliability percentile, highlighting the higher stress induced by the WLTP profile relative to NEDC and JC08.

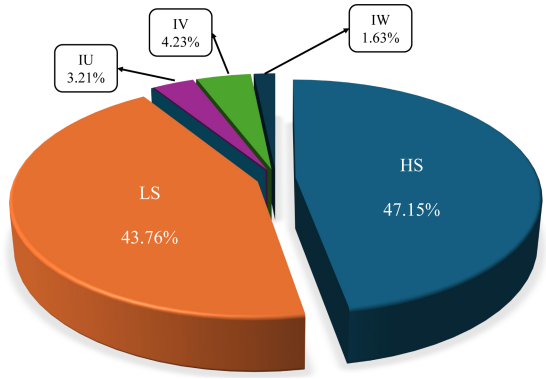


Fig. 30. Contribution to the overall reliability degradation of each data from the mission profile for WLTP cycle at 90% reliability. The HS and LS $T_j$ indicate bond wire degradation, while phase currents IU, IV, and IW contribute to die attach damage.

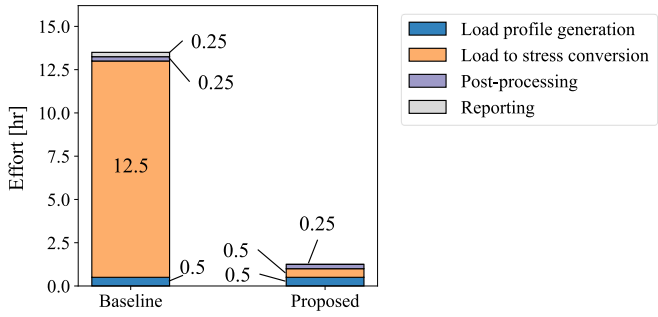


Fig. 31. Estimated effort (hours) comparison in lifetime assessment between the conventional model-based approach and the proposed streamlined test-based approach, excluding setup preparation effort.

The pie chart in Fig. 30 illustrates the contribution of each data point from the WLTP mission profile at 90% system reliability. It is evident from the pie chart that the primary contributions stem from $T_j$ of HS (47.15%) and LS (43.76%), with negligible damage attributed to $T_j$ of HD and LD, and relatively minor contributions from inelastic mechanical degradation due to phase current IU (3.21%), IV (4.23%), and IW (1.63%). It can be concluded that bond wire degradation accounts for the majority (91%) of the SiC module's overall degradation, while the total contribution of die attach damage is 9%.

### *D. Time Reduction in Mission-Profile-Based Lifetime Assessment*

The high-fidelity model-based lifetime assessment effort required for an automotive inverter is taken as the baseline [11] and compared with the proposed streamlined test-oriented lifetime assessment. Estimates for both approaches were obtained in consultation with the automotive industry OEM, based on the time required to assess the targeted drive cycle—here, the WLTP cycle is considered.

The required effort can be divided into the following four categories:

1) mission-profile-to-device-level load profile generation, either via a VSM (baseline) or by executing the drive cycle test through LTL (proposed);
2) load-profile-to-thermal-stressor response creation, using high-fidelity model execution (baseline) or by employing the MML using datasets from LTL (proposed);
3) multiphysics stressor-to-system-level lifetime estimation via postprocessing; and
4) reporting results to the OEM (manual reporting in the baseline approach, automated API reporting in the proposed approach).

The total time for each approach is obtained by summing the durations of these four tasks.

Effort reductions are observed in two categories. Device-level load generation requires equivalent time in both approaches (0.5 h), as both are real-time capable. Load-to-stressor conversion time is reduced from 12.5 h (baseline) to 0.5 h (proposed), as the proposed method eliminates high-fidelity PEC switching transient simulations. Postprocessing time remains the same (0.25 h) since both approaches employ the same lifetime model. Reporting time decreases from 0.25 h to 0 h in the proposed approach, as the report is generated automatically without additional effort, with further savings from streamlined data compilation. In the baseline method for lifetime assessment, the WLTP drive cycle requires 13.5 h, whereas the proposed approach

requires only 1.25 h. Overall, the streamlined proposed approach achieves a 12.25 h reduction (∼90%), as shown in Fig. 31.

## VII. Conclusion

This article proposes a streamlined, test-oriented lifetime assessment framework for automotive PECs that addresses key gaps in current reliability methods. Through the integration of automated test execution, multiphysics cosimulation, mission-profile-specific modeling, and semantic data infrastructure, the framework bridges the divide between accelerated testing and high-fidelity lifetime prediction. Major contributions include: a fully digitalized testing workflow that eliminates manual data-handling bottlenecks, an fully automated automotive inverter test system, which is used to test the inverter across any standard driving cycles, a coupled electro-thermalmechanical model encapsulated as an FMU for integration into system-level analysis, and a combined lifetime model and mission impact assessment approach that quantifies the effect of real-world driving cycles on inverter lifetime and likelihood of failures of inverter systems.

The integration of a multiphysical model significantly improves the accuracy of the prediction by capturing nonlinear interactions among the electrical, thermal, and mechanical domains. The proposed approach is validated using three representative driving profiles: WLTP, NEDC, and JC08. Results reveal substantial variation in both component- and system-level lifetimes as a function of mission-induced stress. At a 99% reliability percentile, the predicted system lifetime under WLTP is only 0.96 million kilometers—substantially lower than the 10.3 million kilometers and 1.75 million kilometers observed under NEDC and JC08, respectively. Additional reliability analysis at a fixed mileage of 480 000 km corroborates these findings, with WLTP yielding a system reliability of 99.54%, compared to 99.96% under NEDC. These findings underscore the critical influence of mission profiles on PEC degradation and highlight the necessity of incorporating mission-aware models in reliability assessment. Furthermore, detailed degradation analysis under WLTP conditions shows that bond wire fatigue, primarily driven by junction temperature fluctuations in high and LS switches, accounts for approximately 91% of the total SiC module degradation, with only 9% attributed to die attach fatigue.

A further key contribution is the substantial reduction in effort required for the proposed streamlined approach. Compared with the high-fidelity model-based baseline, the proposed streamlined test-based approach reduces total assessment time for the WLTP drive cycle from 13.5 hours to just 1.25 hours—a 12.25-h ( 90%) reduction. The most significant savings arise from eliminating time-intensive PEC switching transient simulations. This effort reduction gain not only accelerates design iteration but also facilitates faster decision-making for mission-profile-informed reliability improvements.

The authors envision two distinct directions for future work. First, advancing from conventional overengineering toward mission-profile-informed right-sizing by incorporating enhanced knowledge of component degradation. Second, the development of a deployable application for estimating the remaining useful lifetime, which could be integrated into an edge platform to enable digital twin development for PECs using the established reliability assessment tool.

## Acknowledgment

This work creates a baseline for the ongoing project HiPower 5.0. Views and opinions expressed are, however, those of the author(s) only and do not necessarily reflect those of the European Union, Chips JU, or the national granting authorities. Neither the European Union nor the granting authorities can be held responsible for them. The authors would like to thank Flanders Make for the support to our research group.

## References

[1] M. Company, "Sustainable inclusive powertrain model: Automotive power electronics and harness market outlook," 2023. Accessed: Apr. 18, 2025. [Online]. Available: https://www.mckinsey.com

[2] F. Blaabjerg, H. Wang, I. Vernica, and B. Liu, "Reliability of power electronic systems for EV/HEV applications," *IEEE Trans. Power Electron.*, vol. 109, no. 6, pp. 1060–1076, Jun. 2021, doi: 10.1109/JPROC.2020.3031041.

[3] D. Lee, H.-P. Kieu, J. Kim, S. Choi, S. Kim, and W. Martinez, "A GAN-based improved zeta converter with integrated planar transformer for 800-V electric vehicles," *IEEE Trans. Ind. Electron.*, vol. 71, no. 12, pp. 15815–15825, Dec. 2024.

[4] repairpal, "Toyota Prius Vehicle Recall: The Vehicle May Stall or Operate Only at Reduced Power," Feb. 12, 2014. Accessed: Nov. 19, 2025. [Online]. Available: https://repairpal.com/recall/14V053000

[5] P. Forums, "2017 pacifica hybrid (PHEV) recall: Power inverter module failure due to overvoltage," 2017. Accessed: Aug. 5, 2025. [Online]. Available: https://www.pacificaforums.com/threads/2017-pacifica-hybrid-phev-recall-power-inverter-module-failure-due-to-overvoltage.17810/

[6] electrek, "Tesla recalls over 2,000 cybertrucks to replace inverter that cause loss of power," 2024. Accessed: Aug. 5, 2025. [Online]. Available: https://electrek.co/2024/11/13/tesla-recalls-over-2000-cybertrucks-to-replace-inverter-that-cause-loss-of-power/

[7] C. Reports, "Hyundai, Kia, and Genesis recall EVS that can lose power while driving, again," 2024. Accessed: Aug. 5, 2025. [Online]. Available: https://www.consumerreports.org/cars/car-recalls-defects/hyundai-kia-genesis-recall-evs-that-lose-power-while-driving-a6719394171/

[8] *C. Reports*, "Electric vehicles less reliable, on average, than conventional cars and trucks," 2023. Accessed: Apr. 18, 2025. [Online]. Available: https://www.consumerreports.org

[9] S. Yang, A. Bryant, P. Mawby, D. Xiang, L. Ran, and P. Tavner, "An industry-based survey of reliability in power electronic converters," *IEEE Trans. Ind. Appl.*, vol. 47, no. 3, pp. 1441–1451, May/Jun. 2011.

[10] V. Mulpuri, M. Haque, M. N. Shaheed, and S. Choi, "Multistate Markov analysis in reliability evaluation and life time extension of DC-DC power converter for electric vehicle applications," in *Proc. IEEE Transp. Electrific. Conf. Expo*, 2018, pp. 280–285.

[11] S. Chakraborty et al., "Real-life mission profile-oriented lifetime estimation of a SiC interleaved bidirectional HV DC/DC converter for electric vehicle drivetrains," *IEEE Trans. Emerg. Sel. Topics Power Electron.*, vol. 10, no. 5, pp. 5142–5167, Oct. 2022.

[12] S. Chakraborty, S. K. Bhoi, F. Hosseinabadi, P. Davari, F. Blaabjerg, and O. Hegazy, "X-in-the-loop validation of deep learning-based virtual sensing for lifetime estimation of automotive power electronics converters," *IEEE J. Emerg. Sel. Topics Power Electron.*, vol. 12, no. 6, pp. 5777–5793, Dec. 2024.

[13] Y. Song and B. Wang, "Evaluation methodology and control strategies for improving reliability of HEV power electronic system," *IEEE Trans. Veh. Technol.*, vol. 63, no. 8, pp. 3661–3676, Oct. 2014.

[14] A. Soldati, G. Pietrini, M. Dalboni, and C. Concari, "Electric-vehicle power converters model-based design-for-reliability," *CPSS Trans. Power Electron. Appl.*, vol. 3, no. 2, pp. 102–110, Jun. 2018.

[15] J. Albrecht, T. Horn, S. Habenicht, and S. Rzepka, "Mission profile related design for reliability for power electronics based on finite element simulation," in *Proc. IEEE 25th Electron. Packag. Technol. Conf.*, 2023, pp. 722–726.

[16] J. He, A. Sangwongwanich, Y. Yang, and F. Iannuzzo, "Lifetime evaluation of three-level inverters for 1500-V photovoltaic systems," *IEEE Trans. Emerg. Sel. Topics Power Electron.*, vol. 9, no. 4, pp. 4285–4298, Aug. 2021.

[17] M. Novak, A. Sangwongwanich, and F. Blaabjerg, "Monte Carlo-based reliability estimation methods for power devices in power electronics systems," *IEEE Open J. Power Electron.*, vol. 2, pp. 523–534, 2021.

[18] P. D. Reigosa, H. Wang, Y. Yang, and F. Blaabjerg, "Prediction of bond wire fatigue of IGBTs in a PV inverter under a long-term operation," *IEEE Trans. Power Electron.*, vol. 31, no. 10, pp. 7171–7182, Oct. 2016.
[19] Y. Yang, A. Sangwongwanich, and F. Blaabjerg, "Design for reliability of power electronics for grid-connected photovoltaic systems," *CPSS Trans. Power Electron. Appl.*, vol. 1, no. 1, pp. 92–103, Dec. 2016.
[20] K. Ma, M. Liserre, F. Blaabjerg, and T. Kerekes, "Thermal loading and lifetime estimation for power device considering mission profiles in wind power converter," *IEEE Trans. Power Electron.*, vol. 30, no. 2, pp. 590–602, Feb. 2015.
[21] P. Xu, K. Yang, T. Tang, N. Sun, C. Ye, and W. Song, "Life prediction method for power device of traction inverter in metros," in *Proc. 4th Int. Conf. Smart Power Internet Energy Syst.*, 2022, pp. 624–629.
[22] R. Manikandan and R. R. Singh, "IoT based IGBT power module health monitoring system with RUL estimation for electric drive applications," *IEEE Access*, vol. 12, pp. 118587–118604, 2024.
[23] D. Bhat, S. Muench, and M. Roellig, "Estimation of remaining useful lifetime of power electronic components with machine learning based on mission profile data," *Power Electron. Devices Compon.*, vol. 5, 2023, Art. no. 100040.
[24] *I. T. AG*, "IPOSIM–Power electronics simulation software—Infineon technologies—infineon.com," Accessed: May 5, 2025. [Online]. Available: https://www.infineon.com/cms/en/tools/landing/iposim-infineon-online-power-simulation-platform/
[25] F. Kardan, A. Shekhar, and P. Bauer, "Reliability enhancement of isolated full-bridge DC-DC power converter for fast charging of electric vehicles," *IEEE Open J. Power Electron.*, vol. 5, pp. 1363–1374, 2024.
[26] J. S. Karunarathna, U. K. Madawala, F. Blaabjerg, M. Sandelic, and K. Zhang, "Reliability estimation of wired and wireless fast electric vehicle charging systems," *IEEE Trans. Power Electron.*, vol. 39, no. 12, pp. 15584–15595, Dec. 2024.
[27] J. Albrecht, "Physics-of-failure based lifetime prediction for power electronics under mission profile load conditions," in *Proc. IEEE 26th Int. Conf. Thermal Mech. Multi-Phys. Simul. Exp. Microelectronics Microsystems*, 2025, pp. 1–7.
[28] S. Chakraborty et al., "Scalable modeling approach and robust hardware-in-the-loop testing of an optimized interleaved bidirectional HV DC/DC converter for electric vehicle drivetrains," *IEEE Access*, vol. 8, pp. 115515–115536, 2020.
[29] F. Hosseinabadi, S. Chakraborty, S. K. Bhoi, G. Prochart, D. Hrvanovic, and O. Hegazy, "A comprehensive overview of reliability assessment strategies and testing of power electronics converters," *IEEE Open J. Power Electron.*, vol. 5, pp. 473–512, 2024.
[30] D. H. Collins, A. V. Huzurbazar, and R. L. Warr, "Highly accelerated life testing (HALT): A review from a statistical perspective," *WIREs Comput. Statist.*, vol. 16, no. 4, 2024, Art. no. e70000.
[31] A. Mathew et al., "Investigation of reliability issues in sintered silver interconnected power devices and its lifetime prediction by FEM and experiment," in *Proc. 12th Int. Conf. Integr. Power Electron. Syst.*, 2022, pp. 1–10.
[32] IEEE Reliability Society, "IEEE standard 1332-2012: reliability program for the development and production of electronic products," Inst. Elect. Electron. Eng., Inc., 2013. [Online]. Available: https://standards.ieee.org/ieee/1332/5547/
[33] M. Stender, O. Wallscheid, and J. Boecker, "Comparison of gray-box and black-box two-level three-phase inverter models for electrical drives," *IEEE Trans. Ind. Electron.*, vol. 68, no. 9, pp. 8646–8656, Sep. 2021.
[34] M. Stender, O. Wallscheid, and J. Böcker, "Development of a black-box two-level IGBT three-phase inverter compensation scheme for electrical drives," in *Proc. IEEE 28th Int. Symp. Ind. Electron.*, 2019, pp. 296–301.
[35] C. Byrne and Z. E. und Elektronikindustrie, *Handbook for Robustness Validation of Automotive Electrical/Electronic Modules*. ZVEI–German Elect. Electron. Manufacturers' Assoc.: ZVEI, Jun. 2008. [Online]. Available: https://www.zvei.org/en/subjects/automotive/robustness-validation/
[36] S. Schmid, "Thermal modelling of an IGBT half-bridge module in simcenter amesim and mapping of the system behavior using an artificial neural network," Sep. 2020. [Online]. Available: https://www.linkedin.com/pulse/thermal-modelling-igbt-half-bridge-module-simcenter-amesim-schmid/
[37] R. Dudek, A. Otto, R. Döring, A. Mathew, X. Liu, and S. Rzepka, "Failure prediction and analysis of an IGBT module for industrial applications subjected to passive and power cycling," in *Proc. 24th Int. Conf. Thermal Mech. Multi-Phys. Simul. Exp. Microelectronics Microsystems*, 2023, pp. 1–11.
[38] O. E. Gabriel and D. R. Huitink, "Failure mechanisms driven reliability models for power electronics: A review," *J. Electron. Packag.*, vol. 145, no. 2, 2023, Art. no. 20801.
[39] F. Yang, E. Ugur, and B. Akin, "Evaluation of aging's effect on temperature-sensitive electrical parameters in SiC MOSFETs," *IEEE Trans. Power Electron.*, vol. 35, no. 6, pp. 6315–6331, Jun. 2020.
[40] C. H. van der Broeck, M. Conrad, and R. W. De Doncker, "A thermal modeling methodology for power semiconductor modules," *Microelectronics Rel.*, vol. 55, no. 9, pp. 1938–1944, 2015.
[41] C. H. van der Broeck, L. A. Ruppert, A. Hinz, M. Conrad, and R. W. de Doncker, "Spatial electro-thermal modeling and simulation of power electronic modules," *IEEE Trans. Ind. Appl.*, vol. 54, no. 1, pp. 404–415, Jan./Feb. 2018.
[42] W. D. Leonard Agency in Web Design and W. Strategies, "OTG-F fiber optic temperature sensor, probe and transducer—opsens-solutions.com," Accessed: Aug. 12, 2025. [Online]. Available: https://opsens-solutions.com/products/fiber-optic-temperature-sensors/otg-f/
[43] G. E. Martin, B. Verbrugge, M. M. Hasan, M. El Baghdadi, C. Romano, and O. Hegazy, "Artificial intelligence-driven thermal management in electric vehicle traction inverters: Cooling system optimization and real-time temperature prediction," *IEEE Access*, vol. 13, pp. 167632–167648, 2025.
[44] T. D. Horn, J. Albrecht, and S. Rzepka, "Influence of reducing the load level of mission profiles on the remaining useful life of a to220 analyzed with a surrogate model," in *Proc. PHM Soc. Eur. Conf.*, 2024, pp. 6–6.
[45] *E. G. AQG*, "324: Automotive qualification guideline.," Accessed: Apr. 12, 2025. [Online]. Available: https://www.ecpe.org/research/working-groups/automotive-aqg-324
[46] "General-purpose finite element analysis software," Accessed: Apr. 14, 2025. [Online]. Available: https://www.3ds.com/products/simulia/abaqus
[47] S. K. Hasan, M. Al Ahsan, J. C. Suhling, and P. Lall, "Creep and microstructure evolutions in SAC305 lead free solder subjected to different thermal exposure profiles," in *Proc. IEEE 72nd Electron. Compon. Technol. Conf.*, 2022, pp. 2191–2200.
[48] Q.-L. Xiong, Z. Li, T. Shimada, and T. Kitamura, "Energy storage and dissipation of elastic-plastic deformation under shock compression: Simulation and analysis," *Mech. Mater.*, vol. 158, 2021, Art. no. 103876.
[49] J. Albrecht, T. D. Horn, A. Mathew, R. Dudek, and S. Rzepka, "Development of a reproducible, stable, and scalable evaluation routine for lifetime assessment of power and microelectronic devices based on physics of failure principles," in *Proc. 27th Electron. Packag. Technol. Conf.*, 2025.
[50] M. Musallam and C. M. Johnson, "An efficient implementation of the rainflow counting algorithm for life consumption estimation," *IEEE Trans. Rel.*, vol. 61, no. 4, pp. 978–986, Dec. 2012.
[51] ASTM, *Standard Practices for Cycle Counting in Fatigue Analysis*. Philadelphia, PA, USA: ASTM International, 1999.
[52] A. Wintrich and U. Scheuermann, "An 21-001: Power cycling, lifetime, IGBT modules," Semikron Danfoss, AN 21-001, Jul. 2024.
[53] N. Dornic et al., "Stress-based model for lifetime estimation of bond wire contacts using power cycling tests and finite-element modeling," *IEEE Trans. Emerg. Sel. Topics Power Electron.*, vol. 7, no. 3, pp. 1659–1667, Sep. 2019.



**Sachin Kumar Bhoi** (Member IEEE) received the Master of Technology degree in power electronics from the National Institute of Technology, Tiruchirappalli, India, in 2016. He has been working toward the Ph.D. degree in digital twin for power electronics systems, with Faculty of Engineering Sciences, Vrije Universiteit Brussel, Belgium.

After working in industry for 4+ years in power electronics converter design and simulation for electric vehicles, industrial motor drives and automotive lighting applications, His research interest is specifically focused on developing digital twin frameworks for power electronics applications, targeted toward lifetime assessment and reliability, real-time condition monitoring and prognostic health management. He also has keen research interest in data-driven modeling and simulation of power electronics systems. During his Ph.D. research, he has additionally contributed technically to several activities in EU projects, including the completed HIEFFICIENT and the ongoing EFFEREST and HiPower5.0.



**Sajib Chakraborty** (Member IEEE) received the Ph.D. (with highest honors) in engineering sciences from Vrije Universiteit Brussel (VUB), Belgium, in 2022.

He is currently a Research Professor and the Digital Twin and Reliability (DTR) Team Lead with the EPOWERS Research Group, MOBI Research Center, VUB. He leads research activities within the Power Electronics Reliability Lab (PERL). He serves as technical co-coordinator for five ongoing EU projects—InnoBMS, HARPOONERS, DigiBATT, NEXTBMS, and EFFEREST. He also Leads work packages and VUB-specific tasks in projects, such as HiPower5.0, FlexMCS, SiC4Grid, ZEFES, and eBRT2030. He is the author or coauthor of 90+ scientific publications. His research focuses on cloud-connected and cyber-secure digital twin technologies for power electronics and powertrain systems in automotive, waterborne, and grid applications, including software-defined vehicles (SDV), design-for-reliability, lifetime monitoring and predictive health management, AI-driven modeling, and advanced battery management system hardware (BMS).

Dr. Chakraborty is currently an Associate Editor for IEEE TRANSACTIONS ON TRANSPORTATION ELECTRIFICATION (TTE), a guest editor for *Energies*, and a grant Reviewer for several international funding agencies. He is a Member of IEEE Power Electronics Society and International Scientific Conference on Electric Power Engineering.



**Alireza Aghdaei** (Graduate Student Member, IEEE) received the B.Sc. degree in electrical engineering from the Iran University of Science and Technology, Tehran, Iran, in 2007, and the M.Sc. degree in electrical engineering from RWTH Aachen University, Aachen, Germany, in 2020.

From 2007 to 2017, he was an Electrical Engineer with the energy sector in Iran. He joined the Institute for Power Electronics and Electrical Drives (ISEA), RWTH Aachen University, in 2021 as a Research Associate. His research interests include thermal management and condition monitoring of power modules, degradation diagnosis, reliability of power electronic systems, and real-time health monitoring.



**Anu Mathew** received the M.Sc. degree in micro and nano systems, with specialization in finite element analysis from the Technical University of Chemnitz, Chemnitz, Germany, in 2018.

Since 2018, he has been a Scientific Researcher with the Micro materials Center, Fraunhofer ENAS and TU Chemnitz, Chemnitz, Germany. His main research focus includes reliability analysis and lifetime estimation of power modules, parametric finite element modeling, thermomechanical simulation and optimization of DOEs by FE-program ABAQUS. His current research activities include development of digital twin model for the prediction of lifetime of power devices and reliability analysis on advanced interconnect technology in micro and power electronics by experiment and numerical simulation.



**Tobias Daniel Horn** received the M.Sc. degree in mechanical engineering from the Technical University of Chemnitz, Chemnitz, Germany, in 2016. He is Components Reliability Deputy Group Lead with the Fraunhofer Institute for Electronic Nanosystems ENAS, Chemnitz, Micro Material Center and Technical University of Chemnitz (TUC), Chemnitz, Center for Micro and Nanotechnologies. His research focuses on physics-based condition monitoring for power electronics, including digital shadows for electro-thermomechanical finite element simulations, evaluation methods, counting methods, damage accumulation algorithms and their implementation on microcontrollers.



**Sebastian Liebig** received the Ph.D. degree in power electronics from the Technical University of Chemnitz, Chemnitz, Germany, in 2014.

He was a Developer and Research Project Manager with Liebherr Elektronik, Lindau, Germany, in the field of aerospace power electronics. He joined 2016 AVL-SET, Germany, Wangen, and is currently responsible for the active load cabinet as architect and model designer. Furthermore, he is currently a Project Manager for research projects.

Mr. Liebig was the recipient of the best paper award from PCIM, Nuremberg, in 2011.

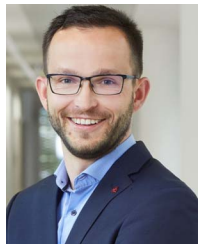

**Jan Albrecht** received the Master of Science degree in mechanical engineering and material engineering from TU Bergakademie Freiberg, Freiberg, Germany, in 2013, and the Ph.D. degree in electrical engineering and information technology from the Chemnitz University of Technology, Chemnitz, Germany, in 2023.

He is currently the Senior Scientist in Mechanical Engineering and Materials Science. Since 2013, he has been a Research Associate with the Micromaterials Department, Fraunhofer ENAS, Chemnitz, Germany. He is a Deputy Head of the Department and Leader of the Research Group Component Reliability. The research work of his group focuses on simulation with special emphasis on lifetime models, fracture and damage mechanics and related material characterization in the field of micro and power electronics.



**Christoph Abart** received the doctorate degree in satellite navigation from the Graz University of Technology, Graz, Austria, in 2009.

He has been a Senior Project Manager with AVL List GmbH, Graz, Austria, since 2017. In this role, he coordinates several nationally and internationally funded research projects in the field of power electronics testing solution for future electric vehicles and energy grids. He was the technical coordinator of the HiEFFICIENT project and now coordinates the follow-up activity HiPower 5.0.



**Rik W. De Doncker** (Fellow, IEEE) received the Ph.D. degree in electromechanical engineering from the KU Leuven, Leuven, Belgium, in 1986.

In 1987, he was a Visiting Associate Professor with the University of Wisconsin, Madison, Madison, WI, USA, where he developed the DAB converter. In 1988, he joined the GE Corporate Research and Development Center, Schenectady, NY, USA. In November 1994, he joined Silicon Power Corporation (formerly GE-SPCO) as Vice President Technology, developing world's first medium-voltage static transfer switch. Since October 1996, he has been a Professor with RWTH Aachen University, Aachen, Germany, where he leads the Institute for Power Electronics and Electrical Drives (ISEA). October 2006, he was a Director of the E.ON Energy Research Center, RWTH Aachen University, where he leads the Institute of Power Generation and Storage Systems. Since 2014, he has been a Director of the German Federal Government BMBF Flexible Electrical Networks (FEN) Research CAMPUS. He has authored or coauthored more than 800 technical papers and is holder of more than 60 patents.

Dr. Doncker was IEEE PELS President in 2005–2006. He was a recipient of the 2002 IAS Outstanding Achievements Award, the 2013 Newell Power Electronics IEEE Technical Field Award, and the 2014 IEEE PELS Harry A. Owen Outstanding Service Award. In 2015, he was also a recipient of Fellow status at RWTH University. In 2016, he became a member of the German Academy of Science and Technology (ACATECH) and the IEEE Medal in Power Engineering in 2020. He has a doctor honoris causa degree of TU Riga, Latvia.



**Omar Hegazy** (Senior Member IEEE) received the Ph.D. degree (with greatest distinction) from the Department of Electrical Engineering and Energy Technology (ETEC), Vrije Universiteit Brussel (VUB), Belgium, in 2012.

He is the Founder and Leader of EPOWERS Research Group (Power Electronics Innovation Lab (PEIL), Powertrain Innovation Lab (PIL), Power Electronics Reliability Lab (PERL) and Smart Charging Lab (SCL), ETEC Department, and MOBI Research Centre, where he coordinates the research activities in this field in several national projects (e.g., via Flanders Make, VLAIO (ex. IWT), Innoviris, Flux50, etc.) and in European projects (e.g., SAFEDRIVE, UNPLUGGED, ELIPTIC, ORCA, ASSURED, HiFi-Elements, GHOST, HiPERFORM, CEVOLVER, OBELICS, ACHILES, LONGRUN, eCharge4drivers, iSTORMY, URBANIZED, HiEFFICIENT, NextETRUCK, SiC4GRID, ZEFES, EBRT2030, OpEVA, NEMOSHIP, NextBMS, ECOMOBILITY, INNOBMS, DIGIBATT, BATTS, EFFEREST, GIANTS, HiPower5.0 etc.). He is also the Manager of MOBI Core-Lab, Flanders Make organization, Leuven, Belgium. He is the author of more than 260 scientific publications and two patent applications. Furthermore, he is an active member of EGVIA, EARPA, Inside (ARTEMIS-IA), EPE, PELS, IES, SAE, and IEC standards. His fields of interest include power electronics, electrical machines, electric and (plug-in) hybrid electric vehicles, digital twin (DT), Reliability and Lifetime, charging infrastructure, power/energy management strategies, FC (Hydrogen) powertrains, battery management systems (BMS), V2X systems, optimization techniques and smart dc grid with renewable energy.